RESEARCH ARTICLE | JULY 23 2024

Hydroacoustic analysis of a full-scale marine vessel: Prediction of the cavitation-induced underwater radiated noise using large eddy simulations

Mohammad-Reza Pendar ; Duncan McIntyre; Peter Oshkai

Physics of Fluids 36, 073331 (2024)
https://doi.org/10.1063/5.0220691

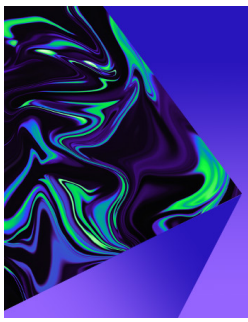

Physics of Fluids ARTICLE pubs.aip.org/aip/pof

Hydroacoustic analysis of a full-scale marine vessel: Prediction of the cavitation-induced underwater radiated noise using large eddy simulations

Cite as: Phys. Fluids **36**, 073331 (2024); doi: 10.1063/5.0220691
Submitted: 28 May 2024 · Accepted: 3 July 2024 ·
Published Online: 23 July 2024

Mohammad-Reza Pendar,[a] Duncan McIntyre, and Peter Oshkai

AFFILIATIONS

Department of Mechanical Engineering, University of Victoria, Victoria, British Columbia V8W2Y2, Canada

[a]Author to whom correspondence should be addressed: pendar@uvic.ca

ABSTRACT

This numerical study provides insight into the mechanism of noise generation by a cavitating flow in the wake of a marine propeller under realistic operating conditions, which poses a significant threat to marine ecosystems. We examined a full-scale vessel with an entire hull and an isolated model-scale marine propeller (INSEAN E779A) with a maneuverable rudder under various highly turbulent inflow conditions that strongly affect the spectral characteristics of the radiated noise. Insight into the acoustic behavior was gained by employing a combination of the large eddy simulation (LES) treatment of turbulence and the Schnerr–Sauer volume of fluid cavitation model. The hydrodynamic solution was coupled with the Ffowcs Williams-Hawkings (FW-H) strategy for noise and vibration identification. We focused on the interactions between the characteristic cavitation patterns of marine propellers (sheet, tip, and hub cavities) and the dominant structures of the turbulent wake (tip, root, trailing edge, and hub vortices, as well as the distributed small-scale vorticity). The small-scale topological structures in the swirling wake of a propeller directly manifest in the radiated sound level and affect the intensity of multiple frequency ranges. Quantitative analysis of thrust, pressure fluctuations, and sound pressure levels (SPLs) demonstrates significant effects of blade loading, wake distribution, and cavitation development. The peak and average SPL distributions obtained through LES show lower dominant and higher average frequencies compared to those obtained by the FW-H method. The overall SPL obtained by LES were higher than those calculated using the FW-H acoustic analogy at all microphone locations. The overall noise was dominated by the low-frequency broadband noise, attributed to energetic helical vortices, and narrow-band peaks in the medium-high frequency range that originated from other sources, like cavitation structures.

I. INTRODUCTION AND MOTIVATION

Underwater radiated noise (URN) in marine environment, particularly shipping, poses a significant environmental threat to ocean life (Bertschneider *et al.*, 2014; Lidtke *et al.*, 2016b). In the past 30 years, maritime activities have led to a rise of 20–30 dB in the natural background noise level of the sea, particularly within the frequency range of 10–300 Hz (Testa *et al.*, 2021; McKenna *et al.*, 2012). This escalation increases the severity of the anthropogenic impact on underwater fauna (Popper and Hawkins, 2016). In 2014, the International Maritime Organization (IMO) approved a technical guideline for commercial shipping noise production (IMO, 2014). The need to predict and control radiated noise and induced pressure fluctuations from ships underscores the importance of the research focus on hydroacoustic modeling in marine engineering. The phenomenological complexities of the involved wakes and cavitation in combination with the limited availability of data from sea trials make prediction of these negative effects a challenging task.

Experimental techniques play a fundamental role in establishing benchmarks of the acoustic signatures of propellers for validation of computational models (Felli *et al.*, 2015; Tani *et al.*, 2017; 2019; and Witte *et al.*, 2019). Wittekind and Schuster (2016) visually observed sheet cavitation patterns around the propeller and measured pressure pulsations around a full-scale ship hull. Full-scale experimental measurements represent the most accurate method for quantifying the noise emitted by vessels. Nevertheless, these measurements are costly (Bertschneider *et al.*, 2014) and are subject to interference from multiple factors.

Conversely, high-fidelity numerical modeling can isolate and distinguish the acoustic signature surface (linear) and volume (non-linear) terms and help identify the regions where the surface terms

dominate over the volume terms and vice versa. Computational fluid dynamics (CFD) tools commonly employ acoustic analogies as an alternative method for assessing both the noise sources and the far-field radiated sound levels. Hydro-acoustic prediction through numerical methods has attracted increasing attention, primarily due to the inherent challenges of conducting hydroacoustic measurements in traditional experimental setups.

Currently, the three numerical methods commonly utilized for noise prediction include approaches based on Lighthill's acoustic analogy (Lighthill, 1952; Williams and Hawkings, 1969; and Lidtke *et al.*, 2016b), computational aeroacoustics (CAA) methods (Ewert, 2008; Ewert *et al.*, 2011), and semi-empirical models (Guo, 2006; Wittekind and Schuster, 2016). CAA methods generally demand significant computing resources, and evaluating the far-field noise using this approach can become unfeasible. Semi-empirical methods demand minimal computational resources and efficiently predict noise; however, their universality is limited (Li *et al.*, 2020).

In focusing on radiated sound rather than the near-field hydrodynamic fluctuations, one would need to solve the flow in an exceedingly large domain with high grid density (Chen *et al.*, 2007). One alternative involves using acoustic analogies based on Lighthill's theory (Lighthill, 1952). Among methods based on Lighthill's acoustic theory, the Ffowcs Williams-Hawkings (FW-H) equation is exceptionally efficient (Williams and Hawkings, 1969; Crighton *et al.*, 1992). This approach uses near-field flow data on a control surface, positioned either on or around the moving solid body, to predict how the generated sound radiate into the far-field. It is particularly effective for analyzing configurations influenced by substantial nonlinear sound sources in the flow field (Brentner and Farassat, 2003; Ianniello *et al.*, 2013).

Hybrid methods based on the FW-H acoustic analogy have become widely utilized and well-developed. These methods are applied where time-accurate turbulence-resolving approaches like large eddy simulation (LES) methods provide the space/time flowfield datasets, from which acoustic sources on the permeable surface are calculated (Mendez *et al.*, 2013; Spalart *et al.*, 2019; and Testa *et al.*, 2021). In this context, nonphysical reflections occurring at the boundaries of the computational domain must be carefully avoided, necessitating precise CFD simulations (Colonius and Lele, 2004). Poinsot and Lelef (1992) demonstrated that numerical boundary conditions, particularly those imposed by the numerical scheme and not directly related to the physics of the problem, have a significant impact on CFD results.

The extensive literature works on handling time-dependent boundary conditions for hyperbolic CFD problems, exemplified by studies such as Rudy and Strikwerda (1980), Thompson (1987), Tam and Webb (1993; 2004), Wells and Renaut (1997), Kurbatskii and Mankbadi (2004), and Colonius and Lele (2004), indicate that compressible CFD solvers, including those used in ship propeller hydroacoustic predictions, can employ well-posed conditions. These conditions ensure non-reflective inflow/outflow boundaries, resulting in physically consistent CFD datasets on the FW-H equation surface.

Salvatore *et al.* (2006) presented a comprehensive integrated hydrodynamic and hydroacoustic model to examine marine propeller cavitation, thoroughly analyzing the noise emissions caused by propeller-induced phenomena. Pan and Zhang (2013) predicted the noise of marine propellers using the formulation developed by Farassat with consideration of non-uniform inflow conditions. They examined the sound pressure directivity characteristics and determined that noise emission is primarily attributed to axial forces. Ianniello and De Bernardis (2015) also employed a similar methodology. Lloyd *et al.* (2015) assessed the Ffowcs Williams-Hawkings (FW-H) acoustic analogy predictive capabilities and compared results with Navier–Stokes solutions. Their findings indicated that the FW-H method aligns closely with direct Reynolds-Averaged Navier–Stokes (RANS) pressure in the propeller plane. However, its accuracy is highly dependent on the accuracy of the input data. Lidtke *et al.* (2016b) employed LES in combination with the Schnerr–Sauer cavitation model and a porous FW-H acoustic analogy to model sheet cavitation over a hydrofoil. This approach permitted them to precisely capture the sound generated monopole nature by an oscillating cavity sheet. Wu *et al.* (2018) employed the k-ω SST turbulence approach with a turbulent viscosity correction, along with the Zwart cavitation model, to simulate the cavitating flow over a propeller. They successfully predicted both cavitation and loading noise using the FW-H acoustic analogy. Kowalczyk and Felicjancik (2016) examined sheet cavitation and tip vortex cavitation occurring on a model-scale propeller subjected to different loading conditions. Through noise measurements, they investigated the hydroacoustic characteristics. They identified the broadband pressure fluctuations source and related sound emissions. Bensow and Liefvendahl (2016) used a scale-resolved LES turbulence model in conjunction with an acoustic analogy to computing radiated noise of five-bladed propellers operating in the wake flow generated by the research vessel Princess Royal hull. Gorji *et al.* (2019) conducted a numerical examination on the influence of skew and rake on hydrodynamic performance and noise level, employing the FW-H equation to predict far-field acoustics at various hydrophone positions using time-dependent pressure data. Results indicated that increasing the rake decreased sound pressure levels (SPLs), while SPL increased for propeller configurations with skew angles up to 45°. However, propellers with higher skew angles exhibited an unexpected jump in SPL. Razaghian *et al.* (2021) numerically investigated the influence of skew, pitch ratio, rake, and blade number on hydroacoustic and hydrodynamic performance under non-cavitating conditions. They considered B-series propeller and used the FW-H method to extract SPLs for each frequency. Their findings indicate that propellers with 5 and 7 blades exhibit favorable SPL. However, increasing the rake angle, geometric pitch angle, and number of blades leads to decreased efficiency. Posa *et al.* (2022) investigated a system comprising an upstream rudder and a downstream propeller, a configuration typical of underwater vehicle propulsion. They employed the direct formulation of the FW-H acoustic analogy. LES computations were performed on a cylindrical grid comprising approximately 1.7×10^9 points. Recently, Yu *et al.* (2023) examined the impact of skew effects on tonal noise generated by full-scale submarine propellers. Their study indicates that skewed propellers produce 9–10 dB less noise in the axial direction while experiencing increased noise emission in specific radiation directions. Wang *et al.* (2023) utilized the SST turbulence model and the ZGB cavitation model to explore how skew angle influences cavitation and low-frequency pressure fluctuations. Through testing four propellers with different skew angles, they observed that increasing the skew angle delays blade cavitation and alters the cavity pattern from sheet cavitation to tip vortex cavitation. Ebrahimi *et al.* (2023) numerically investigated the impact of various endplates on reducing propeller noise, cavitation, and tip vortex. They designed 11 marine propeller

configurations by adjusting endplate orientation, contraction radius, and flap angle. They showed that propellers with contractions of 0.9 and 0.95R, along with a flap angle of 60°, experienced a reduction in sound pressure levels by 5–7 dB compared to the initial propeller, with minimal efficiency loss.

In recent years, there has been considerable debate regarding the relative significance of linear and non-linear sources of sound generated by marine propellers. In the field of aeroacoustics at low Mach numbers, it is widely accepted that linear terms predominantly influence the acoustic signature, and non-linear ones are considered negligible. However, it has been highlighted that this might not always be the case in the realm of hydroacoustics, as it relates to marine propellers (Ianniello, 2016). This complexity adds an additional challenge to the acoustic analysis of marine propellers using computational techniques, as non-linear acoustic sources are situated within the wake flow. Resolving this issue demands very accurate high-fidelity, eddy-resolving methodologies coupled with fine resolutions levels in time and space across a broad range of distances downstream of the propeller plane (Posa *et al.*, 2022). In other words, the necessity to resolve a wide range of scales and to handle highly complex, unsteady wake dynamics is essential for accurate prediction of the URN. Ianniello *et al.* (2013; 2014) investigated both linear and non-linear sources of noise of ships underwater using a Reynolds-averaged Navier–Stokes (RANS) technique. They acknowledged that RANS is not the best option, leading to rapid dissipation of the wake structures and underestimation of the acoustic signature of the non-linear components. Similar recommendations have been made by researchers who conducted RANS computations for various types of marine propellers like the Potsdam propeller (Lidtke *et al.*, 2016a), the propeller of the Seiun-Maru ship (Wu *et al.*, 2018), the Princess Royal propeller (Sezen *et al.*, 2020), and the INSEAN E779A propeller (Sezen *et al.*, 2021). They emphasized the necessity of employing eddy-resolving approaches to more accurately capture the underlying flow physics.

In the more recent study, Ianniello and Testa (2019) showed that in contrast to RANS methods that effectively captured only the linear sound sources from the propeller surface, detached-eddy simulation (DES) was capable of identifying the nonlinear sources originating from wake instability phenomena. More recent works, Ku *et al.* (2021) utilized delayed detached-eddy simulation (DDES) computations to predict the noise resulting from cavitation within the core of tip vortices shed by submarine propellers HSP17 and HSP38. A grid comprises nearly 28×10^6 finite volumes to conduct the primary DDES computations for the entire system. Similarly, Testa *et al.* (2021) and Sezen *et al.* (2020) considered flow over the ship-propeller with a sound concentrating using DES, coupled with a Chimera approach and adaptive mesh refinement technique, respectively.

The sound emitted by a marine propeller is influenced by cavitation, a phenomenon arising from the expansion of small gas nuclei present in the liquid when subjected to tensile stress in low-pressure regions (Plesset and Prosperetti, 1977). In other words, periodic cavitation occurs when the blades of the propeller experience notable fluctuations in hydraulic pressure, inflow velocity fluctuations, and flow structure change. Cavitation noise has received significant attention recently due to its substantial impact on environmental friendliness and concealment (Andrew *et al.*, 2002; McDonald *et al.*, 2006; and Li *et al.*, 2020). Cavitation produces low-frequency noise that can overlap and conceal the communication frequency bands of marine mammals, thereby adversely affecting their normal activities and lives (Hildebrand, 2009). Moreover, cavitation can amplify propeller noise (Aktas *et al.*, 2016; Turner and Kim, 2019), thereby diminishing the stealth of submarines and other naval vessels.

The propeller cavitation and the vibratory excitation forces brought on by pressure fluctuations are the main factors in efficiency losses and propeller-generated noise (Long *et al.*, 2017; Wang *et al.*, 2017; and Wu *et al.*, 2018). Although a well-designed propeller is intended to minimize cavitation, it is likely that some cavitation will still be present, especially when aiming for high efficiency, which is associated with high blade loading (Bensow *et al.*, 2012; Seol *et al.*, 2005). Ji *et al.* (2012) conducted simulations of cavitating flow over a highly skewed propeller and accurately predicted the pressure fluctuations resulting from cavitation and blade rotation. Yu *et al.* (2017) performed a precise simulation of unsteady cavitating flow around a heavily skewed propeller in a non-uniform wake by employing explicit LES, volume of fluid (VOF), and Kunz cavitation model combination. Through this, they identified the factors influencing cavitation and explored the interaction between cavitation structures and vortex formations. In the study conducted by Viitanen *et al.* (2018), the open-water Potsdam propeller was simulated in both wetted and cavitating conditions using delayed DES on an unstructured grid comprising approximately 5.5×10^6 finite volumes. This research is notable for separately computing the surface and volume contributions to the acoustic pressure. Additionally, it provides valuable comparisons between wetted and cavitating conditions.

In this study, we aim to delineate the noise levels generated by marine vessels and assess their impact on mammalian life using high-fidelity numerical hydrodynamic modeling coupled with a hydroacoustic strategy. The adverse effects of ambient anthropogenic noise include masking of the communication and the echolocation signals essential for foraging, predator-prey interaction, growth, and reproduction of marine mammals, as illustrated in Fig. 1 (Houser *et al.*, 2019). In order to mitigate these effects, we perform performed high-fidelity numerical simulations aimed at developing strategies for precisely understanding acoustic signatures of marine vessels.

II. MATHEMATICAL MODEL

A. Governing equations

The continuity and momentum equations take the form of the homogeneous multiphase incompressible Navier–Stokes (NS) equations, which, after applying the Favre-filtering operation, are expressed as

$$\frac{\partial \rho_m}{\partial t} + \frac{\partial (\rho_m \overline{u_j})}{\partial x_j} = 0, \tag{1}$$

$$\frac{\partial (\rho_m \overline{u_j})}{\partial t} + \frac{\partial (\rho_m \overline{u_i u_j})}{\partial x_j} = -\frac{\partial \overline{p}}{\partial x_i} + \frac{\partial}{\partial x_j}\left(\mu_m \frac{\partial \overline{u_i}}{\partial x_j}\right) - \frac{\partial \tau_{ij}}{\partial x_j}, \tag{2}$$

where u_i and p are the velocity component (i-direction) and the mixture pressure. ρ_m and μ_m are the mixture density and viscosity, respectively, which are defined using the liquid (l) and the vapor (v) properties as follows:

$$\mu_m = \alpha \mu_v + (1 - \alpha)\mu_l, \tag{3}$$

$$\rho_m = \alpha \rho_v + (1 - \alpha)\rho_l. \tag{4}$$

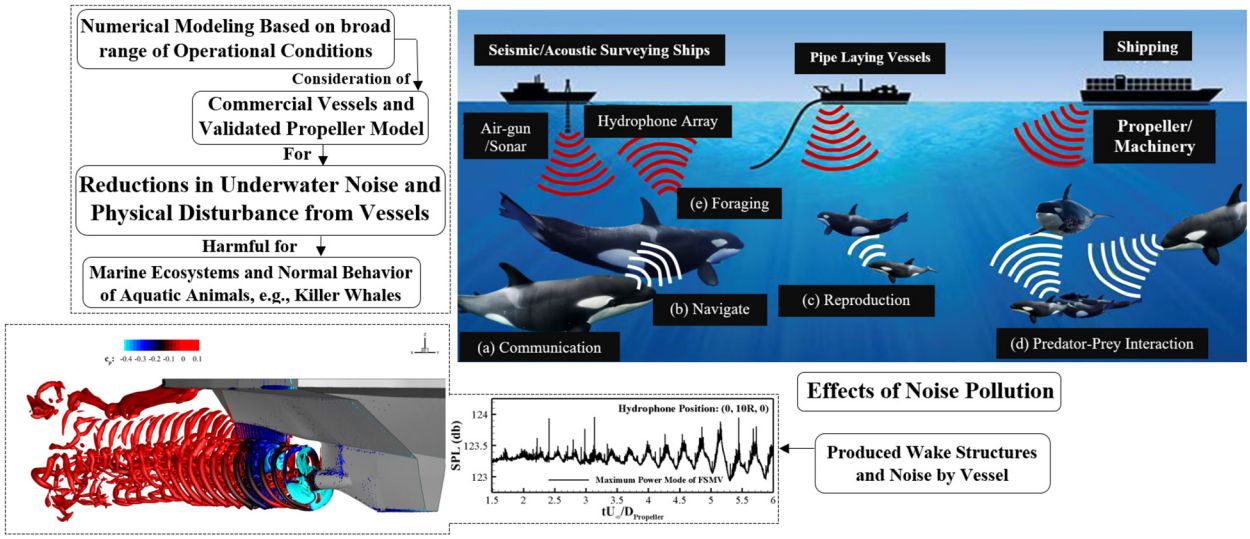

FIG. 1. Schematic representation of anthropogenic hydroacoustic noise sources and their impacts on the life and welfare of mammals.

We applied the LES method of turbulence modeling, which is based on modeling and computing small- and large-scale eddies, respectively. The computation of various components is divided into the grid scale (GS) and the sub-grid scale (SGS). The GS component is $\overline{f} = G * f$, where $G = G(\mathrm{x}, \Delta)$ and $\Delta = \Delta(\mathrm{x})$ are filter function and width (Ghosal, 1996). The unresolved transport component τ_{ij} in Eq. (2), SGS stress tensor, is defined as

$$\tau_{ij} \approx \rho(\overline{u_i u_j} - \overline{u_i}\,\overline{u_j}). \tag{5}$$

This component originates from the filtration of the NS equations and signifies the influence of the unresolved, small scales on the larger, resolved structures of the flow (Bensow and Fureby, 2007). The SGS tensor is modeled using the eddy-viscosity approach as follows:

$$\tau_{ij} = \frac{2}{3}\overline{\rho} k I - 2\mu_k \overline{S_{ij}}, \tag{6}$$

$$\overline{S_{ij}} = \frac{1}{2}\left(\frac{\partial \overline{u_i}}{\partial x_j} + \frac{\partial \overline{u_j}}{\partial x_i}\right). \tag{7}$$

Here, $\overline{S_{ij}}$ is the strain rate tensor, and μ_k is determined by the local eddy-viscosity approach. This study uses an established one-equation eddy viscosity model (OEEVM), and the details of which are described by Pendar and Roohi (2018) and Pendar *et al.* (2023b).

B. Multiphase modeling

A conservative transport equation based on the operated "two-phase mixture" volume of fluid (VOF) strategy was used to track the interface of the vapor cavities

$$\partial_t \alpha + \nabla \cdot (\alpha \vec{v}) + \nabla \cdot [\vec{v}_c \alpha (1-\alpha)] = S_a, \tag{8}$$

$$\alpha = \begin{cases} 1, & \text{liquid (water)}, \\ 0, & \text{gas (vapor)}, \\ 0 < \alpha < 1 & \text{at the interface}. \end{cases} \tag{9}$$

Here, S_α is the rate of phase change between water and vapor. In the modified version of the VOF method implemented within the OpenFOAM framework, called "compressive interface capturing scheme for arbitrary meshes (CICSAM)" (Ubbink, 1997), the interface resolution is enhanced through the introduction of an additional surface compression component [third term on the right-hand side of Eq. (8)], the interface compression velocity ($\vec{v}_c$). Suggested values of the $\vec{v}_c$ are provided in Pendar *et al.* (2020; 2023a).

Schnerr and Sauer formulated a mass transfer model expressed in Eq. (10) (Sauer, 2000; Schnerr and Sauer, 2001). This model is deduced from the Rayleigh–Plesset equation by taking into account the force balance over spherical bubbles

$$S_a = \frac{\rho_v \rho_l}{\rho}(1-\gamma)\gamma \frac{3}{R_b}\sqrt{\frac{2}{3}\frac{|p_v - p|}{\rho_l}}, \quad R_b = \left(\frac{3}{4\pi n_0}\frac{\alpha}{1-\alpha}\right)^{1/3}. \tag{10}$$

The bubble number n_0 in the formula of the bubble radius R_b is set to 1.6×10^9 (Pendar and Roohi, 2018).

C. Acoustic analysis

The FW-H acoustic analogy has been chosen in this study to compute the far-field radiated noise due to its ability to strike a balance between precision and computational efficiency. The FW-H equation takes into account the noise produced by the motion of solid boundaries within the fluid (Williams and Hawkings, 1969), building upon Lighthill's acoustic analogy (Lighthill, 1952). The FW-H equation can be expressed as follows:

$$\frac{\partial^2 p'}{\partial x_i^2} - \frac{1}{c_0^2}\frac{\partial^2 p'}{\partial t^2} = -\frac{\partial T_{ij}}{\partial x_i \partial x_j} - \frac{\partial}{\partial x_i}\left[P_{ij}\delta(f)\frac{\partial f}{\partial x_j}\right] + \frac{\partial}{\partial t}\left[\rho_0 u_i \delta(f)\frac{\partial f}{\partial x_j}\right], \tag{11}$$

where $p' = p - p_0$ represents the sound pressure, c_0 denotes the sound velocity, f is the function related to the sound source surface, with all

points on the surface satisfying $f(x,t)=0$, and $\delta(f)$ is the Dirac function. The stress tensor P_{ij} as well as the Lighthill's stress tensor T_{ij} can be represented as

$$P_{ij}=p\delta_{ij}-\mu\left(\frac{\partial u_i}{\partial x_j}+\frac{\partial u_j}{\partial x_i}-\frac{2}{3}\frac{\partial u_k}{\partial x_k}\delta_{ij}\right), \tag{12}$$

$$T_{ij}=\rho u_i u_j+P_{ij}-c_0^2\rho\delta_{ij}. \tag{13}$$

The three terms on the right-hand side of Eq. (11) refer to the quadrupole, dipole, and monopole sound source terms, respectively. The Farassat 1A Formulation (Farassat and Myers, 1988) introduced a specific integral representation of the FW-H equation to enhance its the versatility, enabling its application to a wider range of cases and making it computationally more efficient. According to Di Francescantonio (1997), this enhancement is achieved by assuming that

$$U_i=\left(1-\frac{\rho}{\rho_0}\right)v_i+\frac{\rho}{\rho_0}u_i, \tag{14}$$

$$L_i=P_{ij}\hat{n}_j+\rho u_i(u_n-v_n). \tag{15}$$

The summation of the monopole (thickness) $P'_T(x,t)$ and dipole (loading) $P'_L(x,t)$ noise source terms results in the total pressure fluctuation terms over time, arising from the turbulent flow and the presence of the solid body

$$P'_T(x,t)=\frac{1}{4\pi}\left(\frac{\partial}{\partial t}\int_{f=0}\left[\frac{\rho_0(\dot{U}_n+U_n)}{r(1-M_r)^2}\right]_\tau dS+\int_{f=0}\left[\frac{\rho_0 U_n\{r\dot{M}_r+c_0(M_r-M)^2\}}{r^2(1-M_r)^3}\right]_\tau dS\right), \tag{16}$$

$$P'_L(x,t)=\frac{1}{4\pi}\left(\frac{1}{c_0}\int_{f=0}\left[\frac{\dot{L}_r}{r(1-M_r)^2}\right]dS+\int_{f=0}\left[\frac{L_r-L_M}{r^2(1-M_r)^2}\right]_\tau dS+\frac{1}{c_0}\int_{f=0}\left[\frac{L_r\{r\dot{M}_r+c_0(M_r-M)^2\}}{r^2(1-M_r)^3}\right]dS\right), \tag{17}$$

where u_i, v_i, r, τ, M_r, and M are the flow velocity, the sound source surface velocity, the distance from the sound source to the observer, retarded time for sound to reach the observer, local Mach number in the $\hat{r}$ direction, and local rotational Mach number, respectively. $u_n=u_i\cdot\hat{n}$, $v_n=u_i\cdot\hat{n}$, $U_n=U_i\cdot\hat{n}$, $L_r=L_i\cdot\hat{r}$, $L_M=L_i\cdot M_i$. The effectiveness of this approach has been confirmed through extensive simulations of far-field radiation noise via marine propellers (Wu *et al.*, 2018; Lidtke *et al.*, 2016b; and Li *et al.*, 2020).

III. SIMULATION METHODOLOGY

A. Computational domain and boundary conditions

Figure 2 presents a schematic illustration of the computational domain, including the propeller, the rudder, and the vessel configurations, along with the associated dimensions and the boundary conditions implemented in this work. This study considers two four-bladed, right-handed, and fixed-pitch propeller geometries at different maneuvering and operational conditions. The first propeller featured four large-size blades with a diameter of $D_{Propeller}=3.8$m that is mounted on the Full-Scale Mainline Vessel (FSMV) [Fig. 2(a)]. The second is the INSEAN E779A propeller with $D_{Propeller}=0.227$m, which is developed at the National Research Council-Institute of Marine Engineering (CNR-INM) (Wang *et al.*, 2021), mounted on a Model-Scale Marine Vessel (MSMV) [Fig. 2(b)]. This propeller geometry has been the subject of many numerical and experimental investigations in the literature (Salvatore *et al.*, 2006), which we used for validation of the present results. For the FSMV configuration, the spatial dimensions of the rectangular computational domain in the x-, y-, and z-directions are $(x/R)\in(-8,8)$, $(y/R)\in(-6,28)$, and $(z/R)\in(-7,3.2)$, respectively. The origin of the coordinates system is established on the propeller center plane. The inflow and outflow boundary were kept at $(y/R)=-6$ and $(y/R)=28$ relative to the propeller's streamwise position. The lateral and depth boundaries were maintained at 8 and 7R from the propeller's axis line, respectively.

The rudder, which is represented by a hydrofoil with a NACA0015 profile, is aligned with the upstream propeller in the free-stream direction for both cases. In the MSMV geometry, the leading-edge (LE) is placed at the $l=0.5D$ from the plane of the propeller, with the chord length equal to $C=0.52D$. For the FSMV body, these values are $l=0.65D$ and $C_{Average}=0.9D$ ($C_{\mathrm{Min}}=0.758D$ and $C_{\mathrm{Max}}=1.21D$), respectively. The hydrofoils are elongated to $h=2.5R$ and $h=2.3R$ in the spanwise direction for the FSMV and MSMV, respectively, to realistically account for the interaction of tip vortices with the propeller slipstream. The clearance between the rudder and propeller is designed to ensure hydrodynamic efficiency, optimize maneuverability, and mitigate vibratory loads associated with blade passage.

Uniform axial velocity, homogenous Neumann, convective, and no-slip wall conditions are imposed on the inflow, lateral, outflow and propeller/vessel body boundaries, respectively (see Fig. 2). Calculations are performed with the imposition of a consistent Courant–Friedrichs–Lewy (CFL) number set to 0.2. This value of CFL sufficiently guarantees the time step size (Δt) within the range of $\approx 1.5\times10^{-5}$–4.5×10^{-5} and $\approx 2\times10^{-7}$–8×10^{-7} for the considered cases of FSMV and MSMV geometries, respectively. The established criterion leads to an occurrence of over 10000 steps per revolution or a rotation of the propeller blades by less than 0.03° per time step (for FSMV), a very high-resolution in time. In all cases, the initial transience diminishes after O (5–10) propeller rotations. The flow evolves during a short period influenced by the initial solution, followed by a time convergence analysis. Subsequently, a quasi-steady state condition is attained and the results are sampled for up to ten computed complete propeller revolutions.

In the discretization of all terms, second-order accuracy is considered, and a convergence target of 1×10^{-6} is employed. In this work, the PIMPLE algorithm—a hybrid of the PISO and SIMPLE algorithms—is used for the pressure-velocity coupling. This approach provides superior stability and a fast convergence rate for higher CFL values and greater coupling applicability, employing PISO for the inner corrector loop and SIMPLE for the outer corrector loop (Pendar and Páscoa, 2019; 2021). The LES modeling in our study employs the wall functions provided by the OpenFOAM package which are activated when $y^+>11$. The residuals for the velocity, pressure, and volume fraction reach approximately 10^{-9}, 10^{-8}, and 10^{-12}, respectively.

To quantify the flow characteristics, especially the noise, different series of discrete microphones are strategically arranged around the

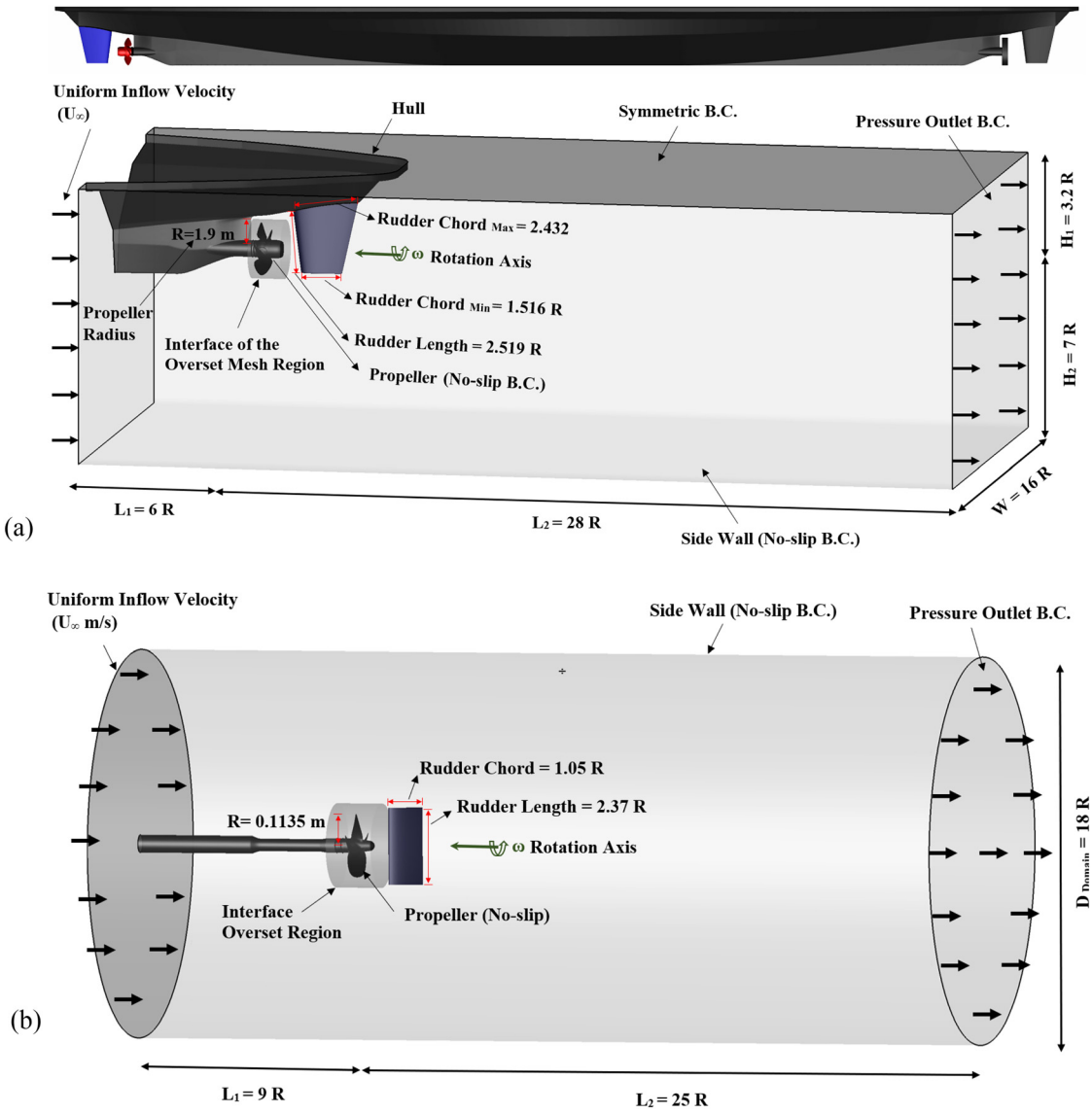

FIG. 2. Three-dimensional perspective of the computational domain and the associated boundary conditions for (a) FSMV and (b) MSMV.

computational domain, over the propeller blade (moving points), and the rudder surface (fixed points) to extract the solution for each time step and expressed FW-H acoustic data. The first microphone series are aligned to investigate the hub (H = 0), tip (H = 0.9R), and far-field (H = 1.8R) [Fig. 3(a)] wake structures over the propeller and the frequency content. Nine specific points are positioned at the tip, leading edge, trailing edge, and center of the blade surface and various radial directions [Fig. 3(b)] for flow analysis. Harmonic analysis of propeller–rudder interaction by quantitative monitoring of probes at the rudder surface is also performed [Fig. 3(c)]. The probes on the rudder surface are positioned at 10%, 42.5%, and 75% of the chord length from the leading edge. Additionally, points on the leading edge and trailing edge are considered.

B. Map of considered cases and settings of approach

The total cases investigated in the current optimization-based study are introduced in Tables I and II. The propeller Reynolds number ($Re_P = \frac{ND^2}{\upsilon}$), hydrofoil Reynolds number ($Re_h = \frac{C_h V_A}{\upsilon}$), advance coefficient ($J = \frac{V_A}{ND}$), and cavitation number ($\sigma_N = \frac{P_0 - P_V}{1/2\rho(ND)^2}$) of considered marine operational conditions are reported in these tables, where V_A, C_h, N, and D are the free-stream velocity, hydrofoil chord, propeller rotational speed, and diameter, respectively. The Reynolds number is calculated by assuming the water kinematic viscosity to be $\nu = 9.0 \times 10^{-7}$ m^2 s^{-1}. In the framework of this study, the FSMV cases are conducted at five various propeller rotational speeds (N_P), ranging from $N_P = 11.9$ to 27.0 rad/s (see Table I). The MSMV cases are

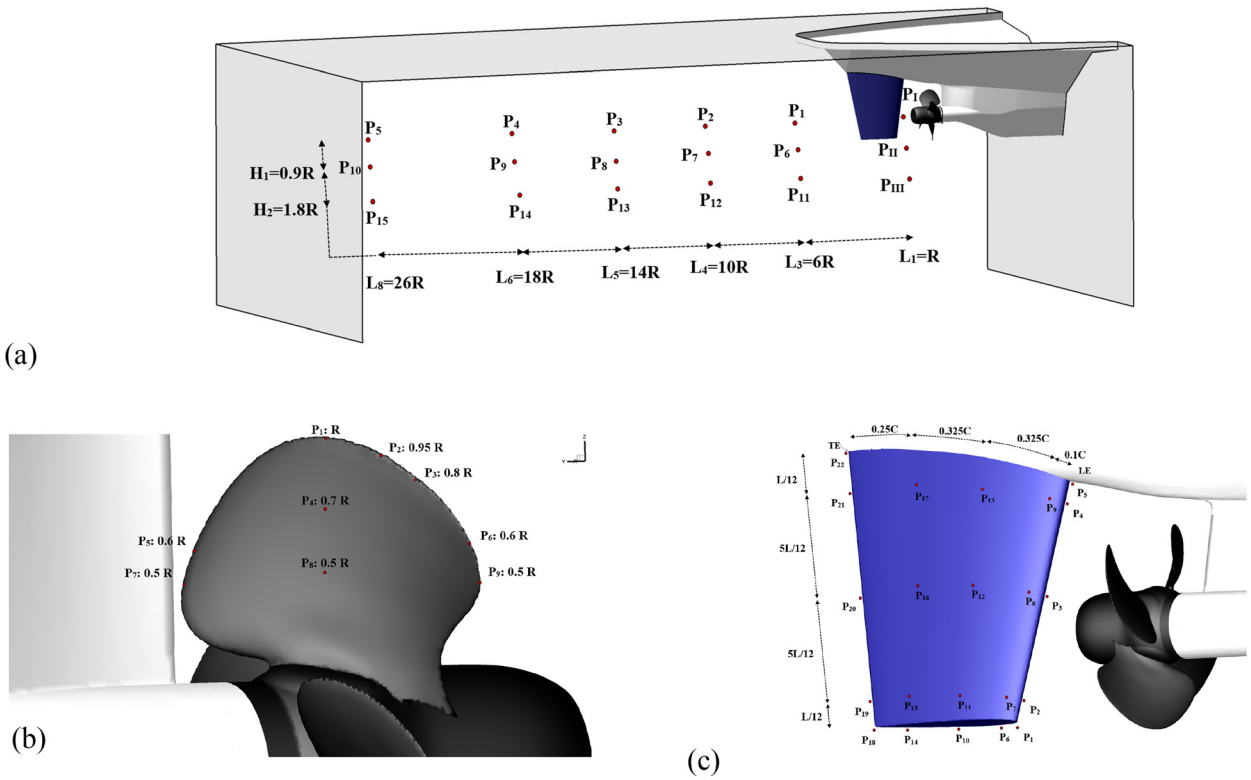

FIG. 3. Schematic drawing of the hydrophone probe locations: (a) listener around the domain, (b) over the propeller blade (moving points), and (c) the rudder surface (fixed points).

TABLE I. Summary of simulations operational conditions for the FSMV geometry.

	Propeller speed (N) (rad/s)	Inlet velocity (V_a) (m/s)	Reynolds (Re_P)	Reynolds (Re_h)	Cavitation number (σ)	Propeller velocity (U_{mag})
FSMV_case1	11.93	8.21	3.06×10^7	3.1×10^7	6.12	22.7
FSMV_case2	15.70	10.80	4.02×10^7	4.1×10^7	3.53	29.87
FSMV_case3	19.47	13.39	4.99×10^7	5.1×10^7	2.29	37.04
FSMV_case4	23.24	15.98	5.95×10^7	6.1×10^7	1.614	44.21
FSMV_case5	27.01	18.58	6.92×10^7	7.1×10^7	1.19	51.38

TABLE II. Summary of simulations operational conditions for the MSMV geometry.

	Propeller speed (N) (rad/s)	Inlet velocity (V_a) (m/s)	Advance coefficient (J)	Cavitation number (σ)	Reynolds (Re_P)	Reynolds (Re_h)	Rudder deflection (α)
MSMV_case1	314.15	8.0	0.71	1.763	2.86×10^6	...	...
MSMV_case2	608.84	11.0	0.50	1.1	5.55×10^6	...	...
MSMV_case3	314.15	8	0.71	1.763	2.86×10^6	1.05×10^6	10
MSMV_case4	608.84	11.0	0.50	1.1	5.55×10^6	1.44×10^6	20

TABLE III. Summary for propellers main parameters.

Quantity	Propeller of MSMV (E779A)	Propeller of FSMV
Propeller diameter (m)	0.227	3.81
Number of blades	4	4
Pitch ratio	1.11	1.32
Hub diameter at prop. Ref. line (m)	0.045 53	1.398
Hub ratio	0.2	0.367
Rake (forward)	4°35′	1°58′
Expanded area ratio	0.689	0.7040
Chord at 0.7R (m)	0.086	1.937

operated at two advance coefficients of $J = 0.5$ and 0.71. Also, to study the impact of rudder angles of attack on vessel maneuverability, three values of rudder angle $\alpha = 0°$, 10°, and 20° are investigated (see Table II). The velocity of inbounding flow is imposed in the range of $V_a = 8.21$–18.58 m/s for the FSMV and $V_a = 8.0$–11 for the MSMV, while maintaining the turbulence intensity (TI) at ≈0.6%. The seawater properties are specified as $\rho_l = 1000$ Kg/m^3, $p_v = 2300$ Pa, $\mu_v = 1 \times 10^{-5}$ kg/m^3, and $\mu_l = 9.7 \times 10^{-4}$ Pa s. Table III displays the geometric parameters of both the FSMV and MSMV (E779A) propellers.

C. Analysis of the computational grid

Figure 4 illustrates the global view of the constructed grids over the computational domain and meridian slices of the grid in different views. Table IV presents a comparative assessment of four discrete grid configurations systematically refined from the preceding coarser level. The results are sampled over ten complete propeller revolutions for the operational conditions of MSMV_case2 and FSMV_case3. The analysis is implemented by monitoring the thrust coefficient ($K_T = \frac{T}{\rho n^2 D^4}$) and torque coefficient ($K_Q = \frac{Q}{\rho n^2 D^5}$) computed on grid levels. It can be observed that with an increase in the number of surface cells, the discrepancy between the considered parameters becomes negligible. Less than a 1% difference between the results of G3_Intermediate_2 and G4_Fine are observed, leading to the selection of G3_Intermediate_2 for our simulations. The total numbers of mesh elements are 15.2×10^6 and 14.1×10^6 for the FSMV and MSMV, respectively. The grid satisfies the LES requirement for grid resolution, with $\Delta L^+ \approx 0.65$ along the near-wall surface (propeller/rudder). This

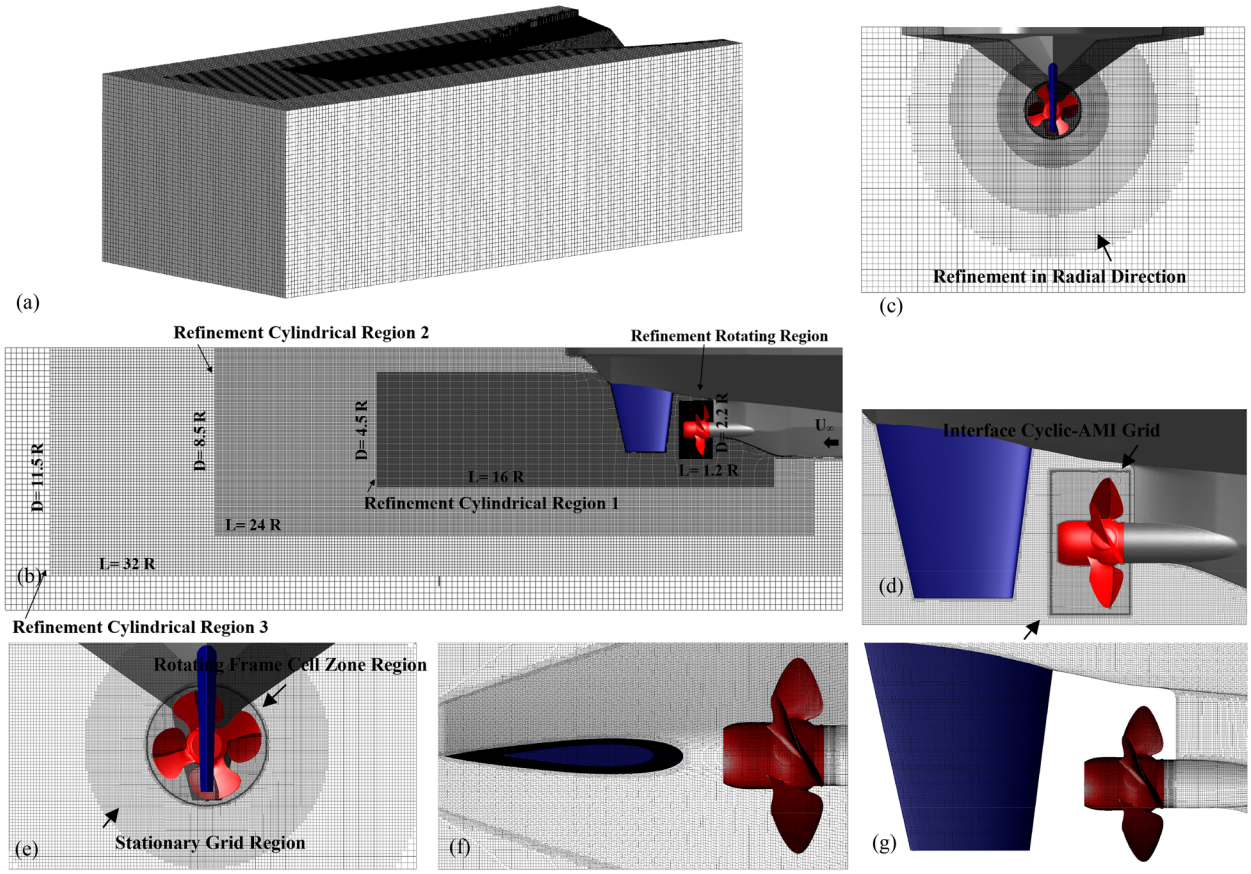

FIG. 4. Three-dimensional mesh generated around the FSMV vessel surface (a). Cross-section planes on the X- axis (b), Y-axis (c) and close-up views of propeller/rudder surfaces, including both rotating and fixed grid regions (d)–(g).

TABLE IV. Examining the impact of four distinct grid resolutions employed in a grid dependence analysis.

	MSMV_case1 ($J = 0.71$), E779A							FSMV_case3			
	Nodes ($\times 10^6$)	Rotor Stator	K_T	$10K_Q$	K_{T_Exp}	$10K_{Q\_Exp}$	Uncertainty of η (%)	Nodes ($\times 10^6$)	Rotor Stator	K_T	$10K_Q$
G1_Coarse	8.1	2.35	0.228	0.449	0.237	0.431	7.660	8.4	1.87	0.231	0.089
		5.75							6.53		
G2_Intermediate_1	10.6	3.45	0.229	0.444	0.237	0.431	6.070	10.7	2.64	0.235	0.088
		7.15							8.06		
G3_Intermediate_2	14.1	4.95	0.231	0.440	0.237	0.431	4.418	15.2	4.89	0.240	0.086
		9.15							10.31		
G4_Fine	17.4	6.10	0.231	0.439	0.237	0.431	4.183	18.6	5.80	0.241	0.085
		11.29							12.80		

resolution is crucial for accurately resolving boundary layers and vortical structures, as depicted in Fig. 4.

Despite the geometric complexity, the SnappyHexMesh tool successfully produces high-quality hexahedral meshes by decomposing computational grids into rotor and stator subdomains managed with the cyclic-arbitrary mesh interface (Cyclic-AMI) technique.

The block-structured grid, employing internal guide cylinders (L = 16, 24, and 32R) is discretized strategically to augment resolution in the vicinity of the propeller blades and rudder surfaces, boundary layers, and in the critical region behind the propeller in the streamwise direction, where vortical structures form higher noise frequency and flow gradient occurs [shown by the cross-section at the midline in

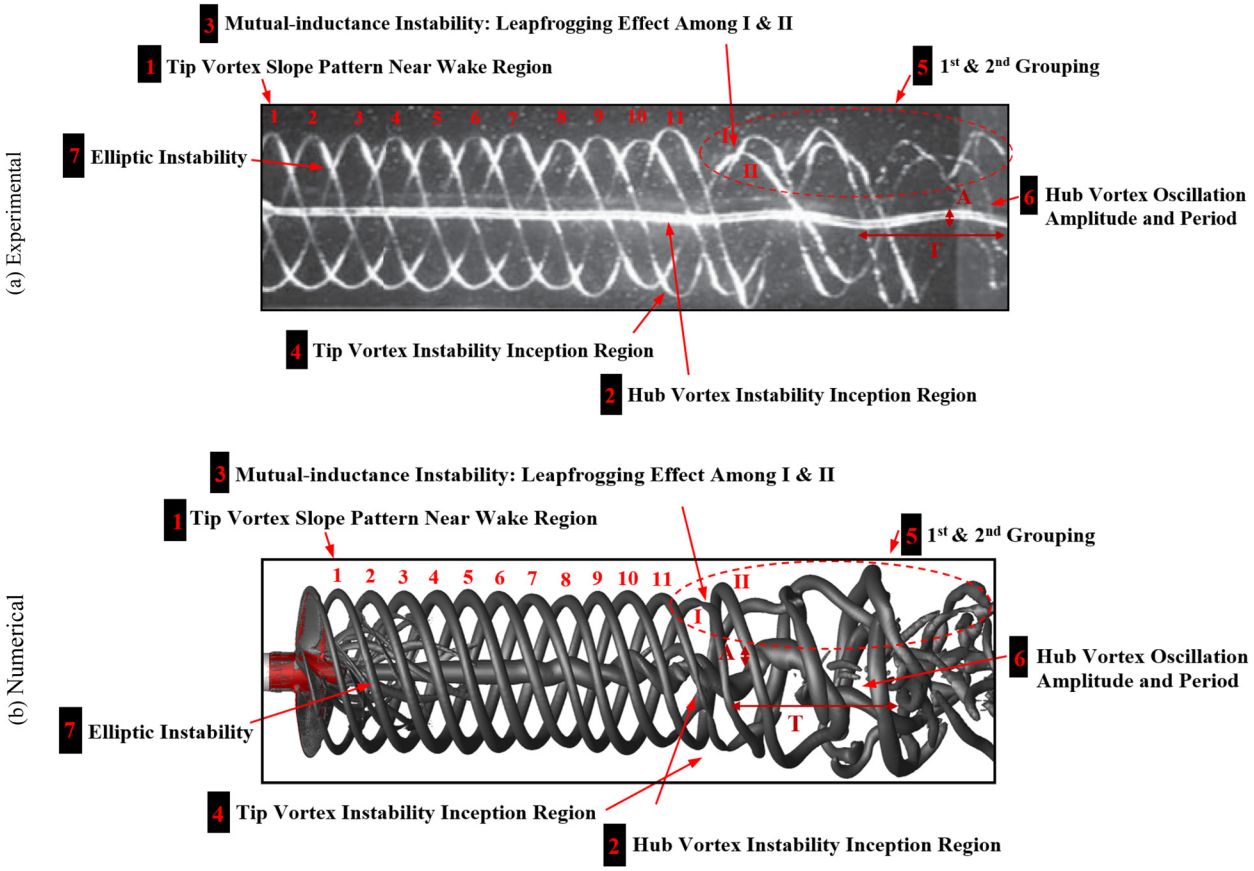

FIG. 5. Propeller wake evolution in advance ratio of 0.75: experimental snapshot (Felli *et al.*, 2011) (a) and current numerical result (b). Identification of tip/hub vortex instability and oscillation; mutual-inductance instability; 1st and 2nd wake grouping.

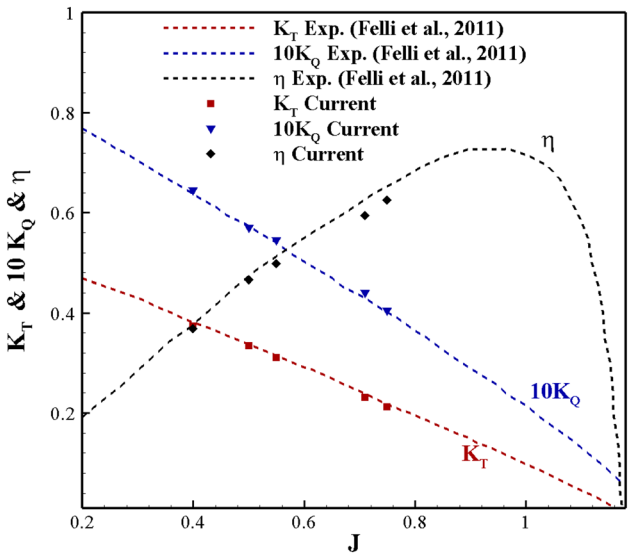

FIG. 6. The solver validation: Comparisons of thrust, torque coefficients, and efficiency for the E779A propeller, with the experimental data (Felli *et al.*, 2011) at different advance coefficients.

Fig. 4(b)]. Additionally, the grid resolution is maximized at the tip region of the propeller and improves at outer radii, extending beyond the tips of the propeller blades [Fig. 4(c)].

Simulations were performed within a high-performance computing (HPC) environment. For instance, the total computational time for the "FSMV_case5" was 864 h when using 144 parallel processor cores. The Kolmogorov length scale (η) is determined, and the grid was confirmed to be sufficiently refined for a well-resolved LES eddies scale, aligning closely with the $-5/3$ slope of the Kolmogorov cascade in front of the rudder and no dominant frequency can be discerned.

IV. CODE VALIDATION

In this section, the precision of the code and numerical strategy are evaluated for validation purposes. The globally reported performance parameters and wake flow fields exhibited excellent agreement with the experimental findings reported by Felli *et al.* (2011) and Salvatore *et al.* (2009). Figure 5 compares the vortical structures obtained from our numerical results employing the Q-criterion and the experimental snapshots reported by Felli *et al.* (2011). The wake topology computed through LES demonstrates a strong qualitative resemblance to the experimental image, accurately capturing features such as tip/hub vortex instability and oscillation, mutual-inductance instability (leapfrogging effect), elliptic instability, and the 1st and 2nd wake grouping. Within the transition wake, a sudden destabilization of tip vortices, which deform from a helical path to interact mutually, forms grouped structures. Likewise, the hub vortex undergoes a deformation from a straight line into a spiraling pattern. In the tip vortices, contraction and divergence destabilization patterns occur following a consistent slope at ≈50% of the maximum length of the tip vortex envelope. The estimated position of this instability occurrence is predicted accurately. Additionally, the correct identification of the hub vortex transition point, where it deviates and incepts to oscillations with a specific amplitude (A) and period (T-one revolution of propeller) before full breakdown occurs, is evident in Fig. 5. The above evaluation and suitable qualitative agreement strongly validate the numerical code and grid system employed in this study for modeling hydrodynamic propeller mechanisms.

In Fig. 6, for various advance coefficient (J) values, numerically obtained values of thrust coefficient (K_T), torque coefficient (K_Q) and propeller efficiency ($\eta = \frac{J}{2\pi}\frac{K_T}{K_Q}$) for the E779A propeller are compared with the experimental data reported by Felli *et al.* (2011). An appropriate agreement is observed in predicting the mentioned coefficients with less than 2% error $[(f_{\mathrm{Exp}} - f_{Num})/f_{Num}]$. The small discrepancy is attributed to measurement errors in the experimental setup and simplifications made in the numerical modeling process.

The region of unsteady cavitation, which appears mainly on the propeller suction side (back side), is compared with the experimental snapshot provided by Salvatore *et al.* (2009) at $J = 0.71$ and $\sigma = 1.71$ in Fig. 7. As evident, our numerical procedure successfully predicts different cavitating phenomena including sheet and hub vortex cavitation as compared to experiments.

V. RESULTS AND DISCUSSION

A. Flow characteristics and vortical structures topology

In Figs. 8 and 9, statistics are presented through the visualization of iso-surfaces of the second invariant of the velocity gradient tensor (Q-criterion; Hunt *et al.*, 1988). Figure 8 compares the wake fields formed under progressively increasing loading conditions with the rudder in a neutral position. As depicted in this figure, the coherence of the tip and hub vortices downstream of the rudder increases with

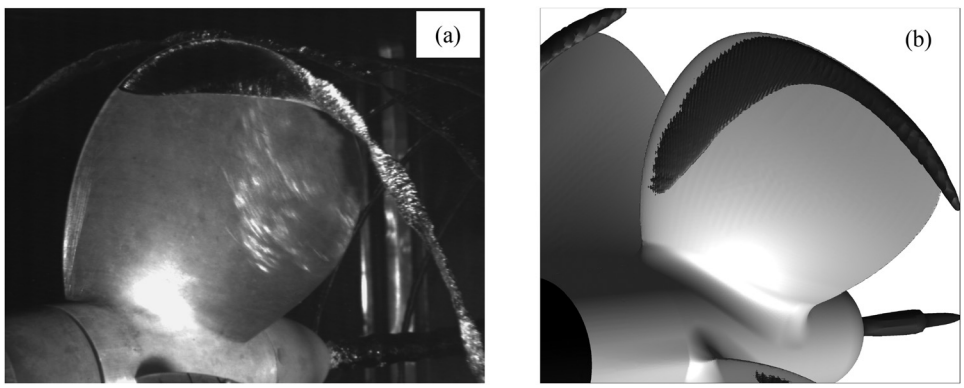

FIG. 7. 3D views of cavitation patters from propeller E779A suction side at $J = 0.71$ and $\sigma = 1.71$: (a) current numerical result, LES/ Schnerr–Sauer models, and (b) experiment of Salvatore *et al.* (2009).

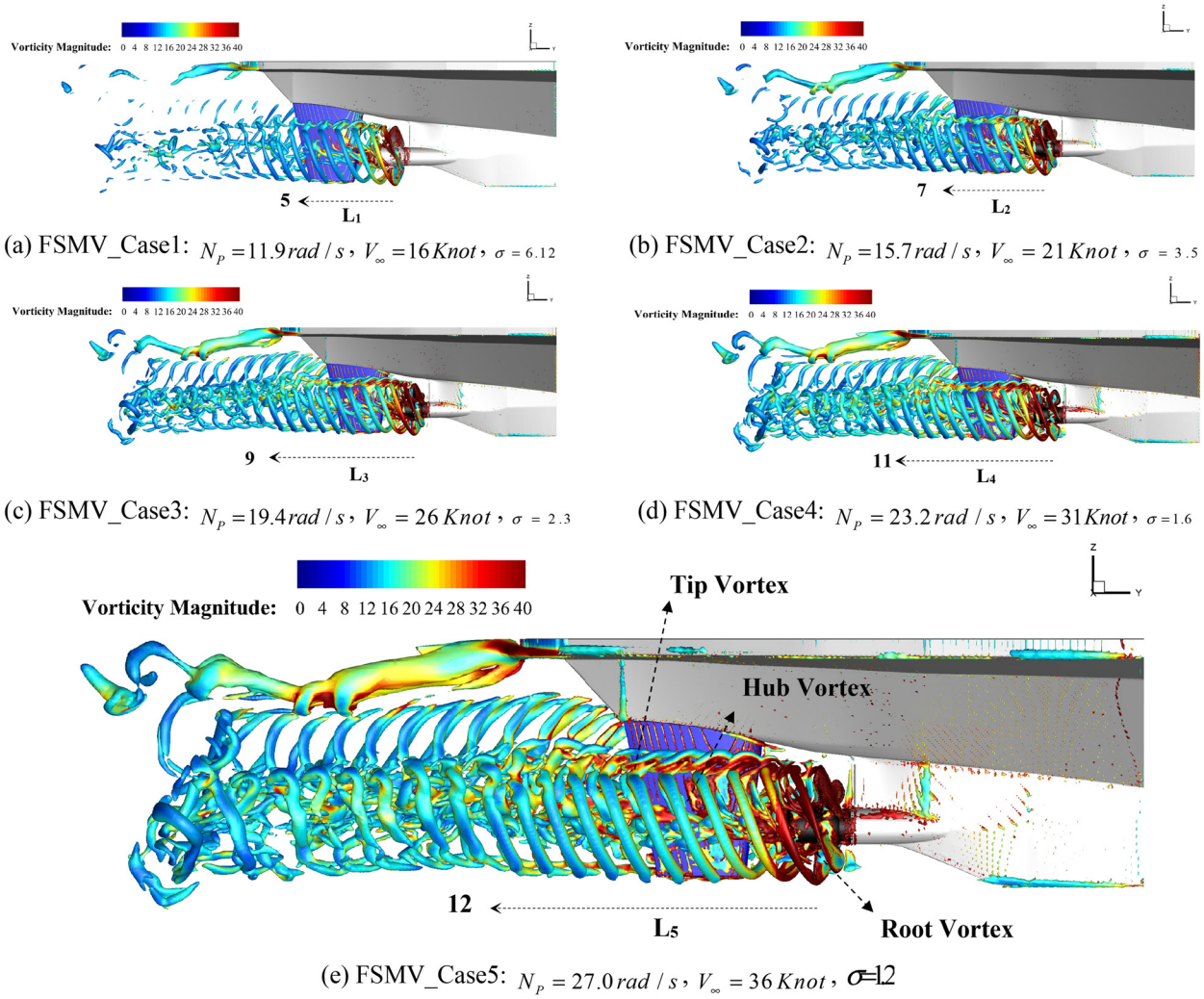

FIG. 8. Iso-surfaces of the second invariant of the velocity gradient tensor with produced helical wake structures density of $Q = 30\,s^{-2}$, colored by vorticity magnitude. Growing load operations: (a) $N_P = 11.9$, (b) $N_P = 15.7$, (c) $N_P = 19.4$, (d) $N_P = 23.2$, and (e) $N_P = 27.0\,rad/s$.

increasing N_P. Additionally, the turbulence destabilization processes added at the accelerated inflow boundary interact with the tip vortices, thereby enhancing diffusion and amplifying the instabilities in the motion of the tip vortices. These two effects are more noticeable under maximized loading conditions, serving as the primary cause for the earlier wake instability observed behind the propeller. Notably, the tip vortices remain coherent further downstream of the propeller compared to the hub vortex. The vortical structures start to oscillate as they undergo the process of breaking up downstream of the rudder. Increased propeller load causes the expansion and fluctuations of wake structures in the radial direction, particularly the hub vortex.

An overview of the differences between propellers operating in conditions with and without downstream rudders in various loads is provided in Figs. 9 through instantaneous Q-criterion Iso-surfaces ($Q = 10\,000\,s^{-2}$), colored with vorticity magnitude. The wake density, chaotic nature, and expansion size all increase both under higher propeller loads ($N_P = 314.15$ to $N_P = 608.84\,rad/s$) [compare Figs. 9(a) and 9(b)] and in the presence of a rudder deflected to a maneuvering angle ($\alpha = 0°$ to $\alpha = 20°$) [compare Figs. 9(a) and 9(c)]. The results demonstrate the dominant impact of loading conditions on the regularity of the wake system [compare Figs. 9(a) and 9(c) with 9(b) and 9(d)]. All vortex patterns—tip, root, trailing edge and hub—are entirely transformed as propeller rotation rate and flow speed are increased. Under the loading condition with lower velocity [depicted in Figs. 9(a) and 9(c)], two key features are observed: (a) an increase in velocity outside the slipstream, leading to a stabilizing effect on the vortex system and (b) quasi-periodic alterations in the vortex core circulation, contributing to a destabilizing influence. The swirling flow and lower pressure induce a more robust vorticity reorganization and recirculation, leading to a transformation of the tip and hub vortex into smaller scale structures. Furthermore, under these conditions, short-standing wake flow features involve the downstream roll-up of the shear layer vorticity shed by blades, giving rise to several

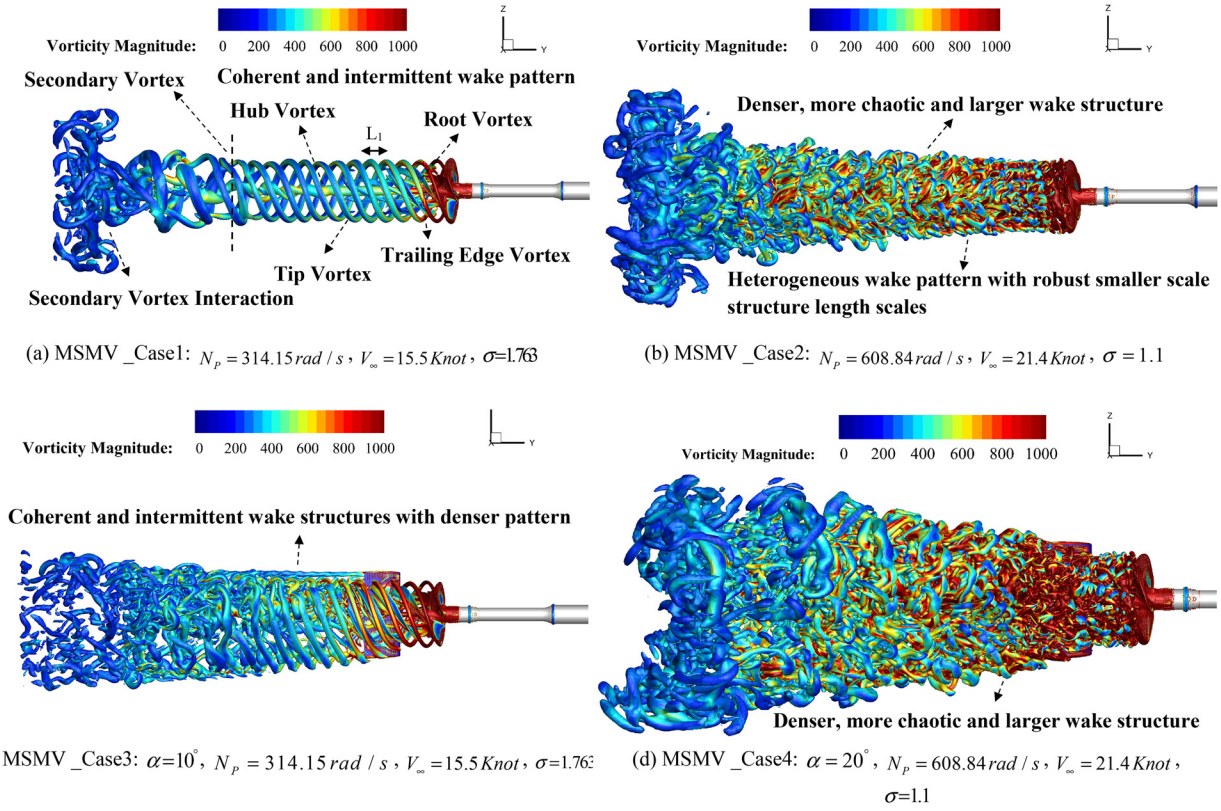

FIG. 9. Vortex field identifications by iso-surfaces of the second invariant of the velocity gradient tensor ($Q = 10\,000\,s^{-2}$), colored with vorticity magnitude. Considerations of load growth from $N_P = 314.15$ (a) and (c) to $N_P = 608.84\,rad/s$ (b) and (d), without (a) and (b) and with (c) and (d) operations of the downstream rudder.

vortices across the span. The direct signature of these turbulent flows is manifested in the radiated sound level produced by the propeller-rudder configuration, which is discussed in the acoustic section.

Figures 10 and 11 depict pressure coefficient contours over iso-surfaces of the second invariant of the velocity gradient tensor. The root vortices disappear due to lower power and weaker pressure minima. The coherent and less intense structure with low-pressure values of tip vortices in case without presence of rudder [Fig. 11(a)] changes into a very dense, irregular and turbulent pattern with larger pressure in case with rudder ($\alpha = 10°$) [Fig. 11(b)]. The hub vortices generate local pressure minima and are more likely to develop cavitation and associated noise in all considered cases.

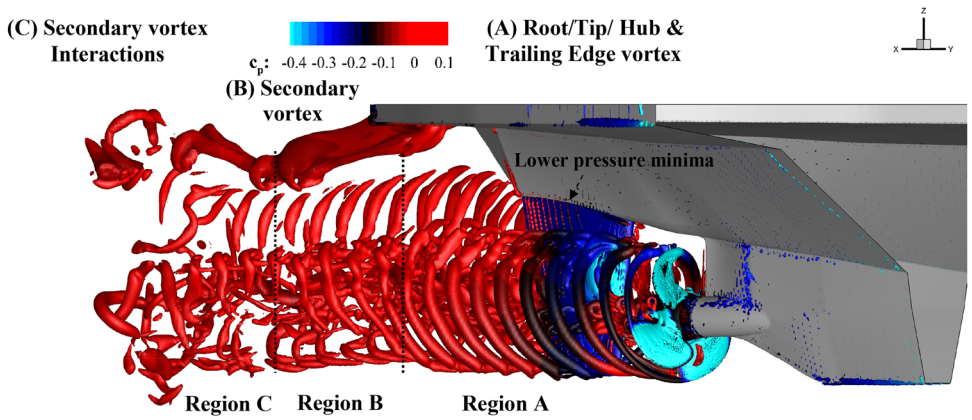

FIG. 10. Visualizations of the pressure coefficient contour through 3D iso-surfaces of the second invariant of the velocity gradient tensor (Q), density of the helical structures are $Q = 30\ s^{-2}$ for FSMV_case5 ($N_P = 27.0\,rad/s$).

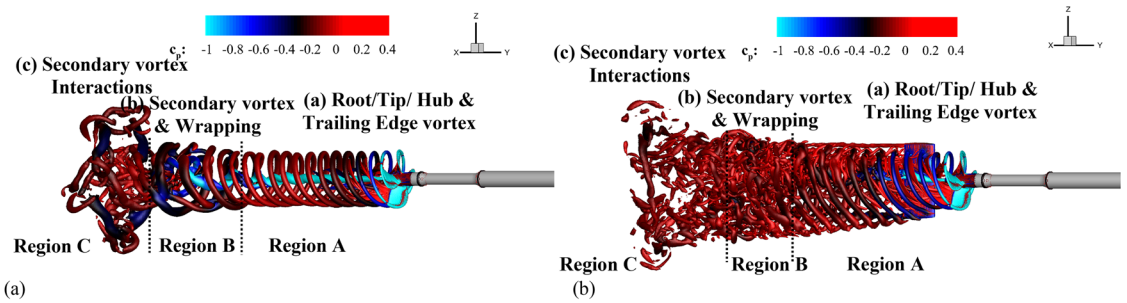

FIG. 11. Evolution of vortical structures formation, visualized by iso-surfaces of the second invariant of the velocity gradient tensor ($Q = 10\,000\,s^{-2}$), colored by pressure coefficient values (C_P) [$N_P = 314.15\,rad/s$, $\sigma = 1.763$, $Re = 2.86 \times 10^6$, and $V_\infty = 8\,m/s\,(15.5\,Knot)$]. (a) MSMV _case1, (b) MSMV _case7: $\alpha = 10^\circ$.

In Figs. 10 and 11, the instantaneous wake vortex systems, which mainly consist of the hub, tip, root, and trailing edge vortices are illustrated. For the convenience of analysis, the wake is divided into stable (region A), transient (region B), and unstable (region C) regions. The tip vortices and hub vortex exhibit notable strength and persist well far downstream. Contrastingly, the trailing edge vortex demonstrates earlier dissipation and breakdown. In region A, inflow turbulence alters the regular spiral tip vortices' wake topology, leading to circumferential local distortions, particularly in downstream evolution, that disrupt the balance of the tip vortex system. In Region B, the distorted vortices form a secondary vortex pattern that wraps around the tip vortices in the circumferential direction during downstream evolution. They begin to bridge the adjacent tip vortices and reduce the gap between them, resulting in further tip vortex distortion. The rapid

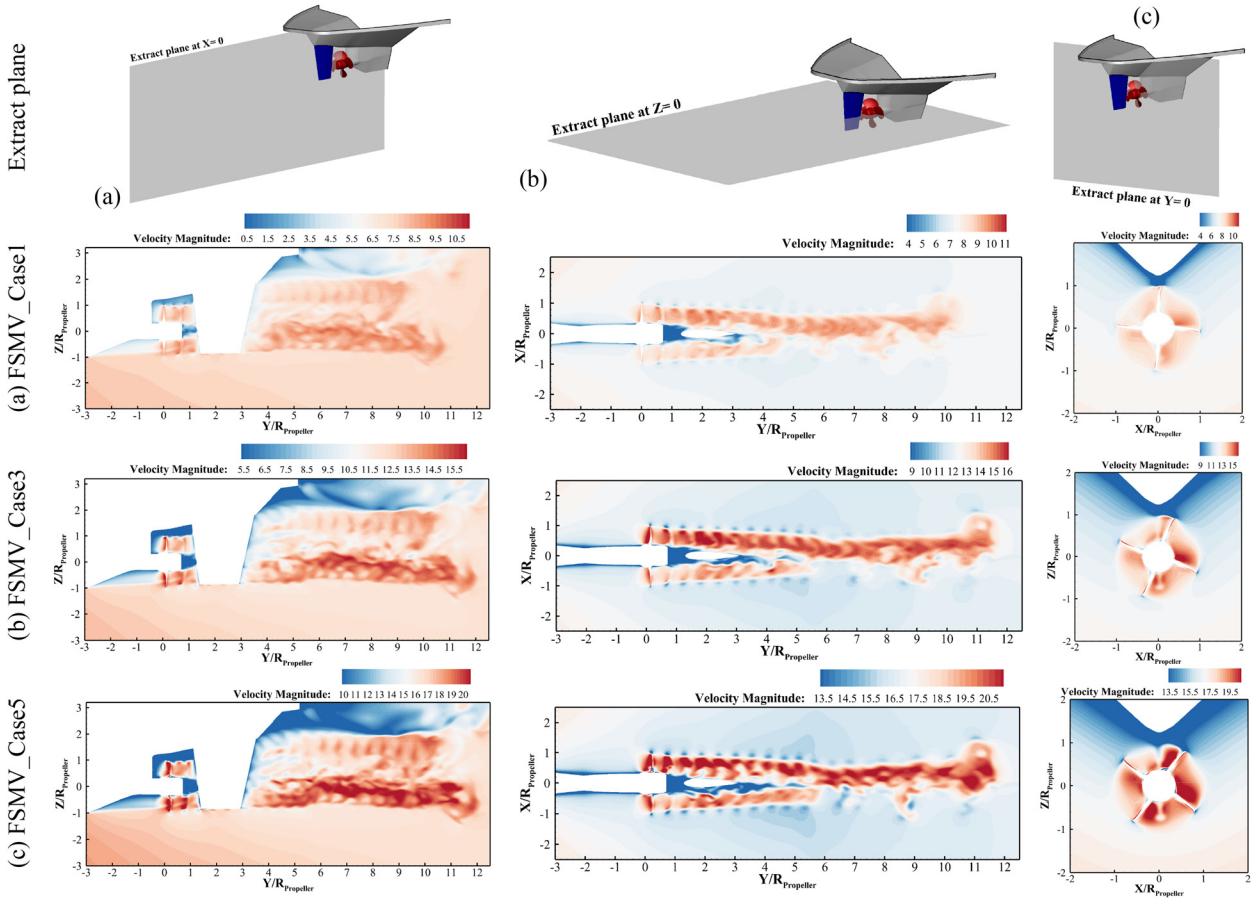

FIG. 12. Evolution of the velocity magnitude contours extracted at the (a) X-plane of X = 0, (b) Z-plane of Z = 0 and (c) Y-plane of Y = 0, for three operational scenarios, FSMV_case1, case3, and case5.

disintegration of vortex structures into smaller scales makes it challenging to observe the behavior of tip vortex pairing. The interaction between numerous secondary vortices leads to their breakdown into small-scale vortices. In Region C, complex small-scale vortex structures with significant dynamic behaviors dominate. In this region, coherent wake structures are not distinguishable at all. The separated, multi-rotating vortex structures propel the upstream tip vortex toward the high-speed shear layer located at the inner radius of the propeller wake.

In Fig. 12, velocity magnitude planes at three distinct axes—X = 0, Z = 0, and Y = 0 directions— are depicted to offer deeper insights into the propeller wake pattern captured by the LES. These details show the connections that facilitate energy transfer between the physical fields behind adjacent blades, reinforcing the interference effect between neighboring tip vortices. Due to this energy dissipation in the helical wake structures, radial expansion is experienced for both hub and tip vortices in all operational conditions (see Fig. 12). The maximum velocities are observed in the lower semicircle of the vortex structure in FSMV_case5, corresponding to the region where the propeller blades generate maximum thrust. Conversely, comparably lower velocities are experienced in the upper semicircle of the vortex structure, closer to the surface, in all cases. The inner wake exhibits a velocity deficit, particularly prominent within the hub vortex region, which leads to expand downstream. The velocity pattern at the X-plane [Fig. 12(a)] indicates that the diameter of the helical wake pattern, after passing over the rudder, is approximately 1.5 times larger than the distance between the propeller and rudder. The upper view at Z = 0 [Fig. 12(b)] illustrates the narrowing of the wake pattern due to the inward velocity of the wake as it passes over the rudder. As tip vortices mature and form pairs, the diffusion of vorticity leads to the generation

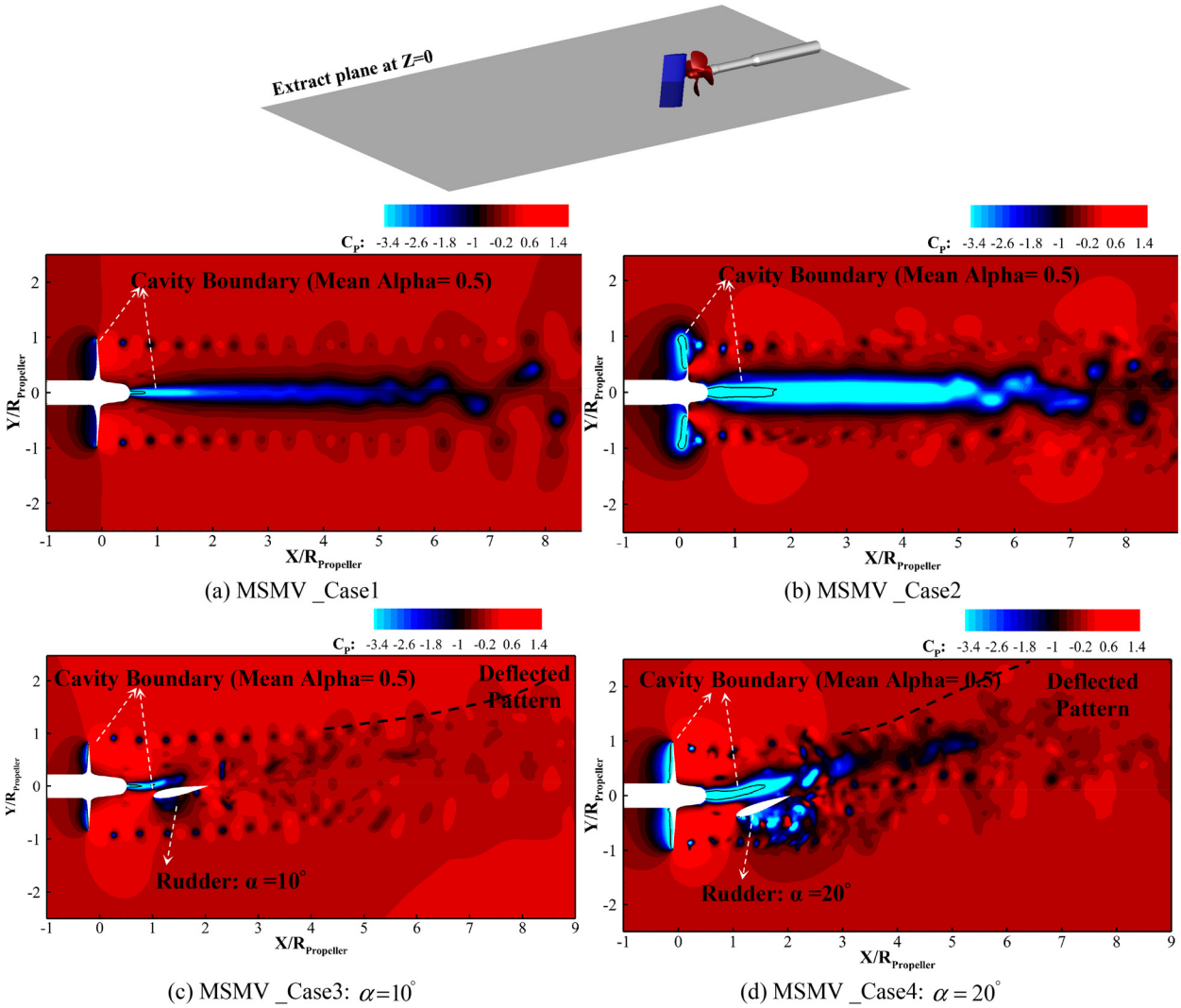

FIG. 13. Visualization of the pressure coefficient contour extracted on the horizontal plane at Z = 0: (a) $N_P = 314.15$, $\alpha = -$, (b) $N_P = 608.84$, $\alpha = -$, (c) $N_P = 314.15$, $\alpha = 10^{\circ}$, and (d) $N_P = 608.84\, rad/s$, $\alpha = 20^{\circ}$.

of negative azimuthal velocity at the outer edges of the wake. Toward the end of the detected wake, stability is entirely compromised, leading to its enlargement and distortion.

To emphasize the distinct interaction of the tip and hub vortices with the rudder, the pressure coefficient fields over the horizontal plane are presented in Fig. 13. The swirl within the wake of the propeller, characterized by an azimuthal velocity component, induces a substantial spanwise pressure gradient across both surfaces of the rudder. While moving across the chord of the hydrofoil, the coherence of the tip vortices tends to diminish compared to their upstream positions. The anti-symmetric topology of the tip vortices becomes evident at the higher angle of the rudder. In Fig. 13, the solid black lines show the mean cavity region borders ($\alpha_v = 0.5$). A substantial expansion of the cavity with increased propeller velocity is evident, encompassing both the hub cavity and sheet cavitation on the blades. The introduction of the rudder markedly deflects the hub cavity. Figure 14 depicts contour plots of velocity magnitude on the Z = 0 plane. The maximum axial velocity manifests at around 0.7R, playing a crucial role in generating propeller thrust. In all scenarios, the time-averaged axial velocity profile illustrates the velocity deficit and radial expansion caused by the downstream wake instability along with the significant interference among the vortex structures. The radial expansion of the vortex strip indicates that the mutual inductance effect between individual tip vortices has become more influential.

The time-varying thrust and torque coefficients under different cavitation simulation scenarios ($1.2 \leq \sigma \leq 6.1$) are depicted in Fig. 15 and Table V. In all plots, the x-axis is normalized by the freestream velocity (U_∞) and propeller diameter ($D_{Propeller}$). The disparity in thrust between the maximum (780 kN) and minimum (292 kN) values of the propeller at rotational speeds of $N_P = 27$ and $N_P = 11.9\ rad/s$,

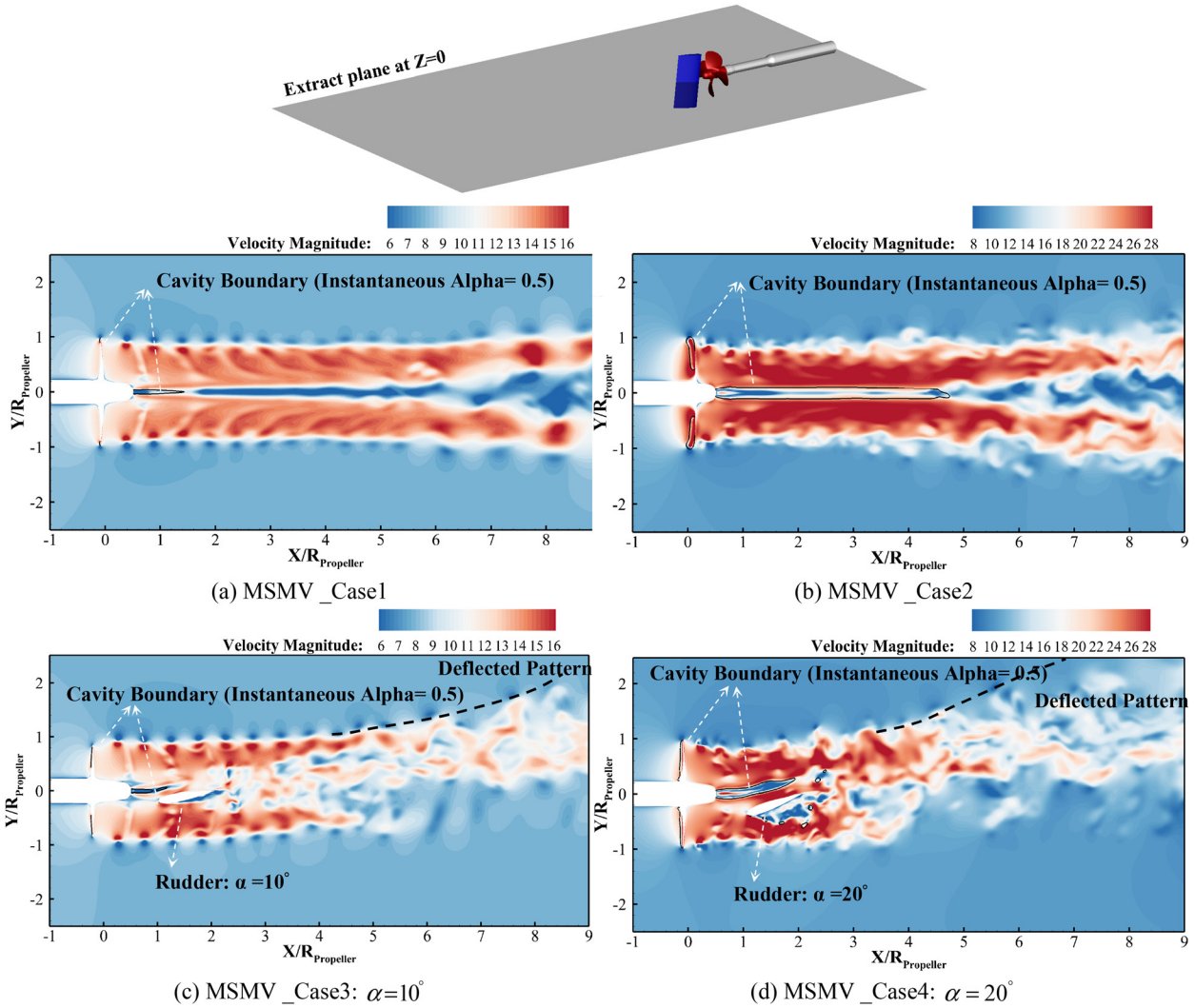

FIG. 14. Visualization of the velocity magnitude on the horizontal plane at Z = 0: (a) $N_P = 314.15$, $\alpha = -$, (b) $N_P = 608.84$, $\alpha = -$, (c) $N_P = 314.15$, $\alpha = 10^\circ$ (d) $N_P = 608.84\ rad/s$, $\alpha = 20^\circ$. (e) Slice of the 3D field where the flow quantities are extracted.

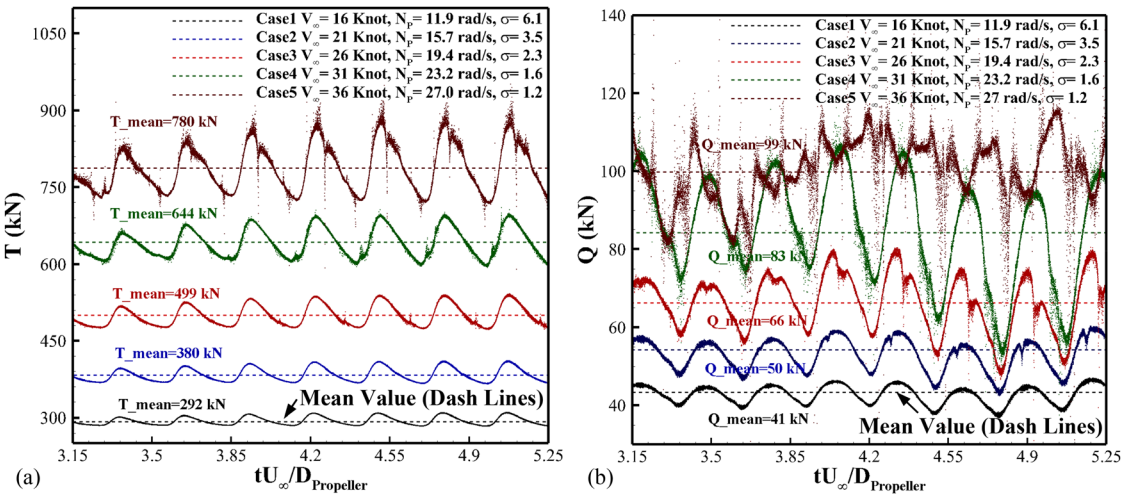

FIG. 15. Time history of the thrust (a) and torque (b) values under different cavitation simulation scenarios. Dashed lines denote their respective mean values.

respectively, is notable. However, the variance in the thrust-to-torque coefficient ratio (K_T/K_Q) stands at 2.8. The periodic features can be observed and the deviation of the load fluctuating from their mean values is minimal under these flow conditions. The overall patterns of thrust and torque amplitudes experience significant growth, despite exhibiting nearly identical periods across five distinct loading conditions. Also, more irregular patterns are observed for the forces, particularly torque, under heavier load conditions. One of the notable occurrences in maximizing load conditions is cavitation in FSMV_case5, which optimizes the overall propeller performance. This observation is supported by similar findings in the literature, as demonstrated by Hu *et al.* (2021).

The time-evolving contours of the cavitation regions, represented by the iso-surface of vapor volume fraction ($\alpha_v = 0.5$), are depicted in Fig. 16 for FSMV_case5 and FSMV_case4. Sheet cavitation on the forward propeller initiates from the leading edge and extends to the tip. Under higher propeller loads, the lower cavitation number directly manifests itself in the increased noise intensity in the axial direction. Because of the strong vorticity within the flow, shed cavities appear to roll up together to create a dense vortex above the blade surface. The monopole sound pressure is directly linked to vapor volume acceleration and exhibits quasi-periodicity in the time domain. It iss crucial to emphasize that significant immediate monopole noise is induced during the cavitation collapse stage in the more violent cavitation conditions of FSMV_case5. This happens because the local cavitation volume undergoes more rapid changes during cavitation collapse, which in turn causes a relatively large vapor volume acceleration, generating instantaneously strong acoustic monopole sources.

TABLE V. Summary of time-averaged load values for the Full-Scale Mainline Vessel (FSMV) under different operational conditions.

	K_T	K_Q	K_T/K_Q	T (kN)	Q (kN)
FSMV_case1	0.3870	0.0142	27.184	292.78	40.99
FSMV_case2	0.2899	0.0101	28.543	380.12	50.68
FSMV_case3	0.2475	0.0086	28.655	498.83	66.25
FSMV_case4	0.2242	0.0076	29.431	643.95	83.27
FSMV_case5	0.2010	0.0067	29.985	779.65	98.95

Figure 17(a) presents the vapor volume fractions (α_v) for FSMV_case4 and FSMV_case5 at the blade tip (r = R) recorded by a non-fixed probe under the condition of rotating microphones together with the blade surface. After experiencing a large sheet cavity, a partial collapse occurs, leaving behind only a small amount of vapor. Comparing volume fraction (α_v) data for all cases at the tip (r = R) and leading edge (r = 0.95R) [Fig. 17(b)] of the blade reveals that with an increase in the cavitation number accompanied by the growth of environmental pressure, the extent of the cavity diminishes considerably. A larger cavitation area, forward of propeller, was observed in FSMV_case5 ($\sigma = 1.2$) compared to FSMV_case1 and FSMV_case2, where almost no cavitation was observed. These distributions demonstrate the occurrence of disparate cavitation dynamics, resulting in multiple frequencies as indicated in acoustic analysis thereafter. Our noise analysis indicates that the influence of the tip vortex on the radiated noise from the propeller may be particularly significant for receivers positioned downstream, playing a key role as a primary broadband noise contributor, especially when there is significant cavitation in the vortex core.

B. Frequency analysis

The noise performance of the FSMV is evaluated using microphones positioned at specific axial distances (L = R, 6R, 10R, 14R, 18R, and 26R) from the propeller source, considering three radial series of r = 0, 0.9R, and 1.8R [see locations at Fig. 3(a)]. Figure 18 depict a quantitative analysis of the pressure fluctuations at these points for radial distances of r = 0, 0.9R, and 1.8R. It is observed that the periodic pressure fluctuation occurs synchronously at all points, attributed to effects such as the development of vortical structures and cavitation. The receiver points located at an axial distance of R from the blade source, as located in the region between the propeller and rudder, exhibit chaotic behavior attributed to the complex nature of the local

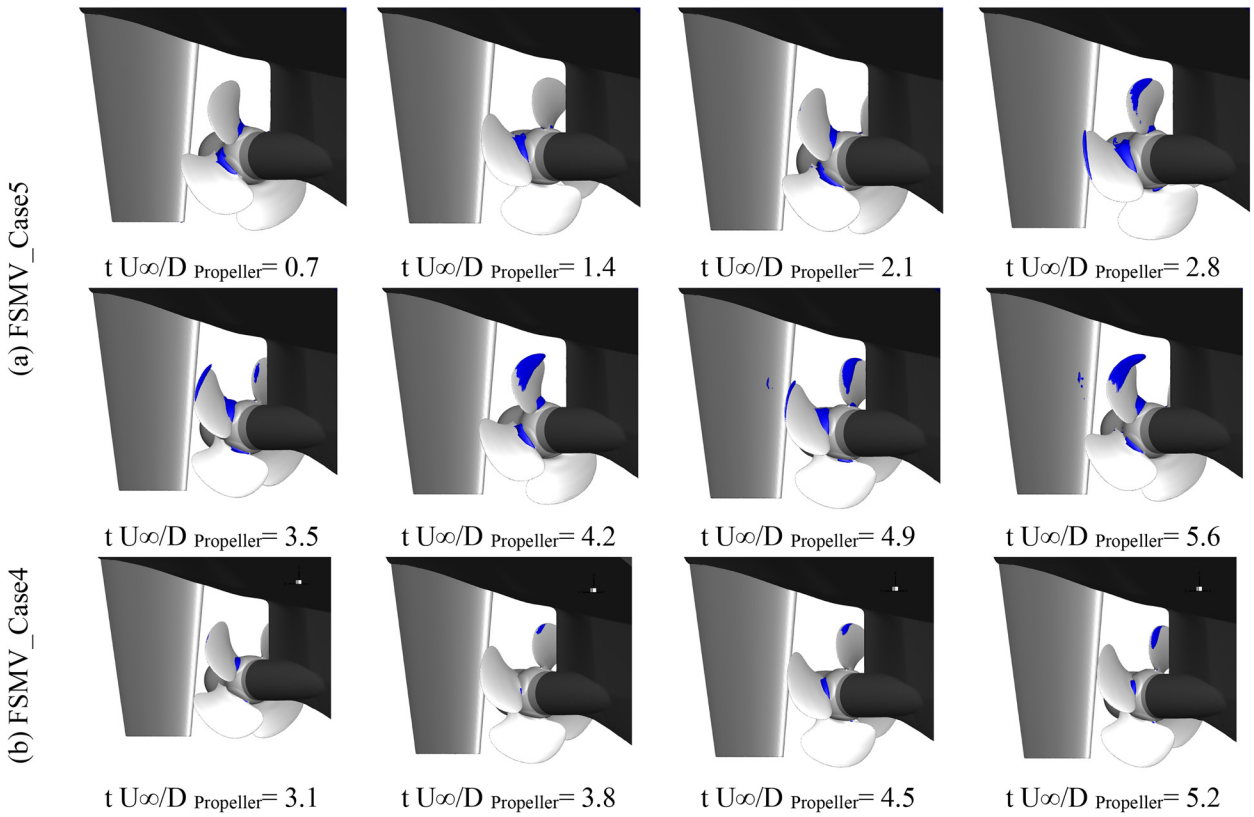

FIG. 16. Evolution of the cavitation pattern during the propeller rotation for the FSMV_case5 ($\sigma = 1.2$) and FSMV_case4 ($\sigma = 1.6$).

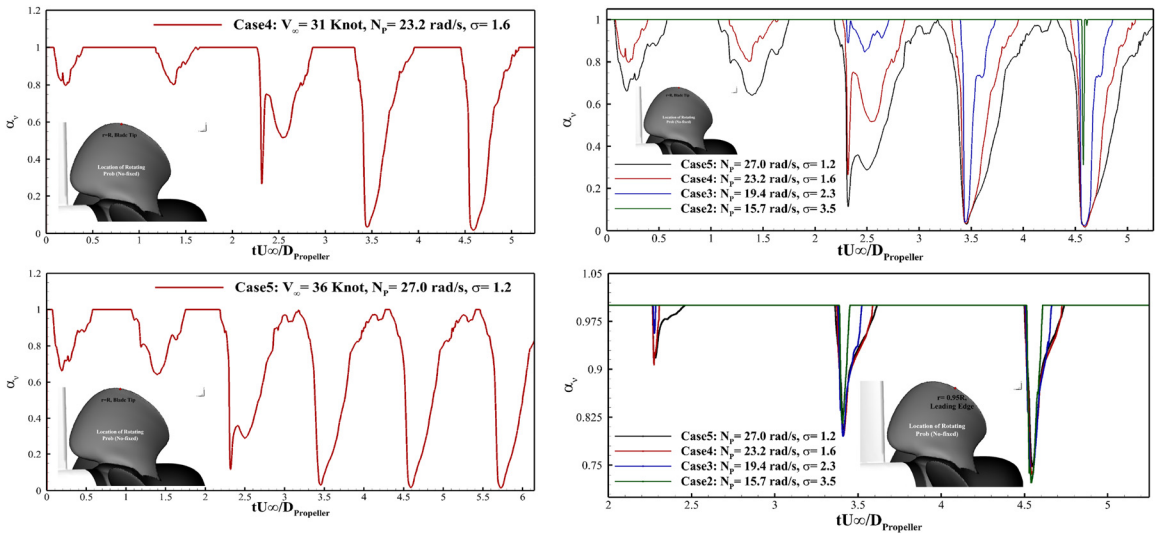

FIG. 17. Distribution of the recorded volume fraction (α_V) distributions for (a) FSMV_case4 and case5 at the tip (r = R), and (b) comparison of all cases at the tip (r = R) and leading edge (r = 0.95R).

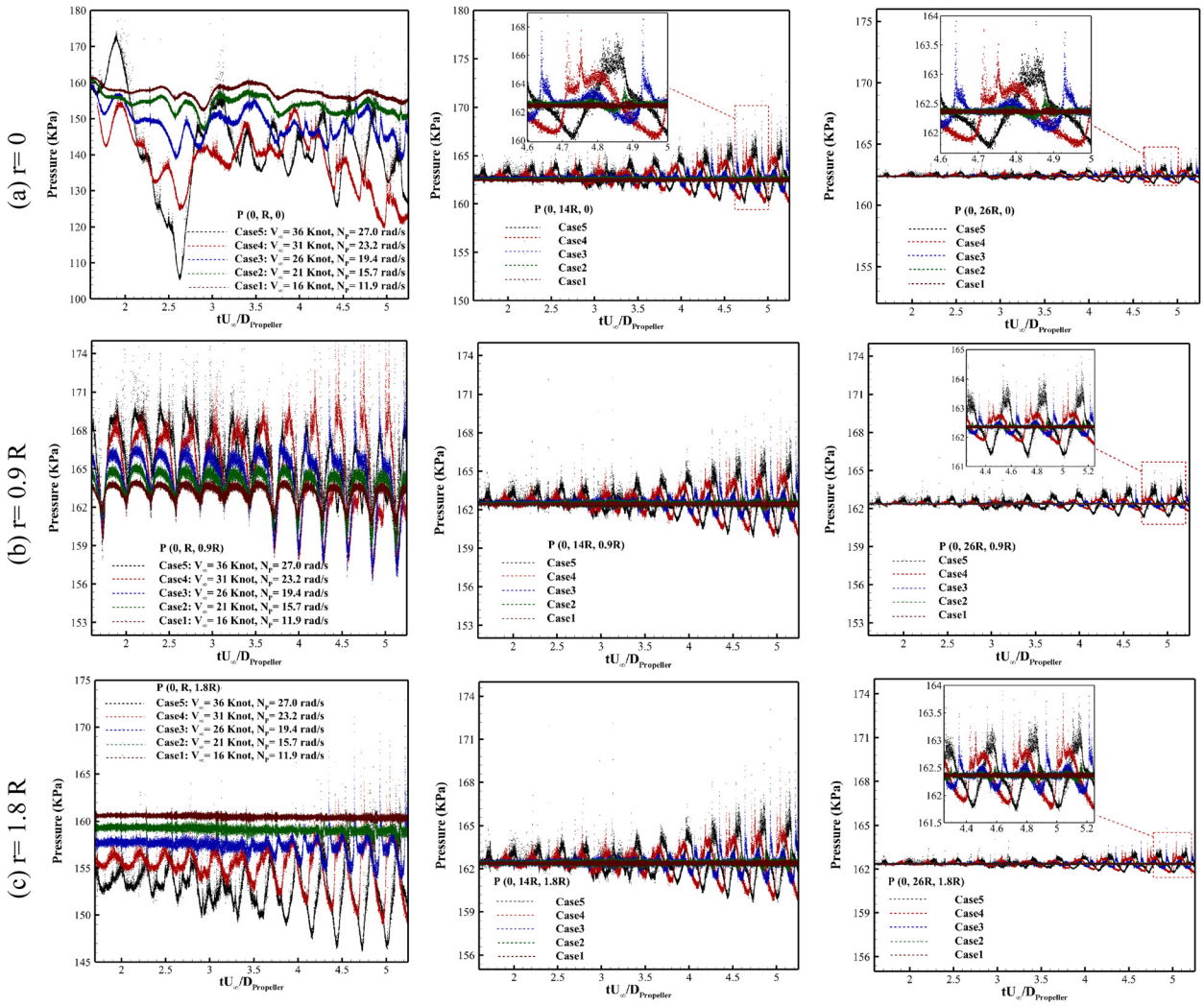

FIG. 18. Pressure fluctuations recorded for five loading scenarios of the FSMV_case 1–5 at radial proximity (a) r = 0, (b) r = 0.9 R and (c) r = 1.8R across three axial intervals of L = R, 6R, 14R, and 26R.

high turbulence multi-phase flow. The pressure evolution in all other frames clearly show that increasing the blade load of the vessel is correlated with an increase in the amplitude of pressure fluctuations. The pressure fluctuation induced by the cavitating flow field constitutes one of the primary sources of vibrations and noise. For microphones positioned at r = 0 [Fig. 18(a)] and r = 0.9R [Fig. 18(b)], the local vortical structure results in greater pressure fluctuation at the hub and tip vortex regions, respectively. As the distance from the main noise source of the propeller increases from 6R to 26R, the total pressure values exhibit a slight decrease, while the pressure fluctuations decline significantly.

Figure 19 shows the pressure fluctuation on the suction side of the propeller blade at specific moving microphones, with detailed locations depicted in Fig. 3(b). Due to the non-uniform wake distribution upstream of the propeller, pressure undergoes substantial fluctuations at various locations, particularly near the blade tip region, showcasing notable disparities among the different cases. The distribution within the propeller tip region suggests that pressure fluctuations may exhibit reduced sensitivity to volumetric changes of the vapor cavity in certain instances. The temporal variation in cavity volume could be interpreted as a sink/source pair. The highest values of pressure are achieved at r = 0.8R and r = 0.6R due to intense tip vortex instability. Pressures decrease toward the lower radii due to the decrease in tip vortex' instability. At the blade tip, a pressure drop occurs due to cavitation, particularly evident in cases with higher rotational speeds [Fig. 19(a)]. Contrasting pressure trends are also observed for the microphones positioned at the blade's leading edge (LE) and center are clearly evident in cases depicted by frames e and f in Fig. 19.

Our time history analysis for FSMV-case 5 and 4 reveals that the second derivative of the volumetric cavity closely follows the pressure coefficient pattern, exhibiting nearly in-phase behavior. Since the acoustic emissions resulting from a periodic sink/source are perceived

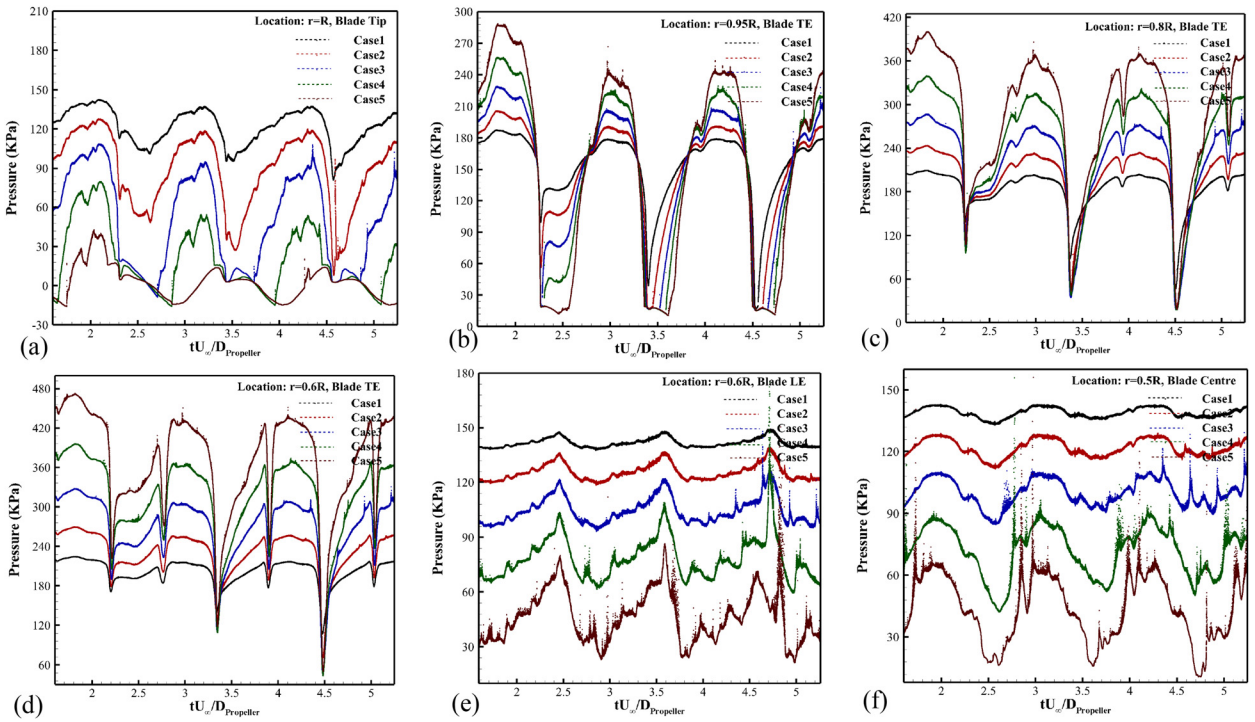

FIG. 19. Illustration pressure fluctuations at different locations on the propeller blade surface for FSMV_case 1 to 5; (a) r = R, blade tip, (b) r = 0.95R, blade TE, (c) r = 0.8R, blade TE, (d) r = 0.6R, blade TE, (e) r = 0.6R, blade LE, and (f) r = 0.5R, blade center.

as monopolar, the monopole source contributions to cavitation noise are attributed to the time variation in cavity volume.

The FW-H analogy transports the pressure variations from the near field to the far field. LES coupled with the FW-H analogy is an appropriate framework for predicting the broadband noise spectrum, as it can effectively capture unsteady phenomena. Figures 20 and 21 compare the true sound of the LES simulation with the sound pressure levels (SPLs) obtained by the FWH predictions up to 34.79 kHz for five different loading conditions at three radial series of r = 0, 0.9R, and 1.8R. The SPL, determined by $SPL = 20\log_{10}(p_{rms}/p_{ref})dB$, where p_{rms} denotes the root mean square of the fluctuating pressure time history and $p_{ref} = 1\mu Pa$ is the reference pressure, is captured by various microphones positioned at the axial distances (R, 26R) in these radial distances. This analysis elucidates the relationship between acoustic noise and vessel loading conditions. In Fig. 20, the peaks of sound pressure oscillation frequencies at various propeller rotational speeds demonstrate discernible variations in patterns, decreasing as N_P increases. Similar trends are observed across all microphones within different cases, albeit with differing values, in both FW-H and LES data. These figures illustrate that the predominant noise and peaks are concentrated within the low-frequency regimes. Therefore, a comprehensive analysis of noise primarily focuses on the salient features within the 0–1000 Hz range. Significant alterations in the narrow-band spectral characteristics were observed across different speed regimes, particularly for frequencies below 100 Hz. Variations in flow dynamics and cavitation seems mainly influence these evolving characteristics and changing features. For frequencies exceeding 200 Hz, the frequency spectrum curve exhibits more stable fluctuations. Several narrow peaks in higher range of frequency were observed.

One contributing factor to the increased noise at higher N_P is the augmentation of cavitation noise, as illustrated by the distribution of cavitation in Fig. 16. As cavitation noise tends to be louder in the low-frequency regions, at higher frequencies, all cases exhibit more similar sound pressure patterns. The narrow-band peaks observed in the medium-high frequency range typically originate from general sources, including common cavitation structures, background noise, or artifacts resulting from filtering and correction processes. While distinct variations indicative of different loading conditions is observed over the broad spectral features, in the higher frequency range, certain portions of the spectral features remained unaffected by operational changes.

In the FW-H method, the influence of the non-linear (quadrupole) terms, particularly noticeable in lower frequencies, along with the predominant effect of the linear terms, collectively contribute to the overall noise levels. This non-linear term influences the overall spectrum shape, making it differ in slope from the linear part. The observed behavior clarifies that the source of the noise continues downstream primarily due to the wake contribution, while the generated noise by radiation from the propeller surface reduces with distance. As indicated by the analysis of turbulent wake structures behind the propeller, helical vortices serve as the primary source of non-linear terms in the noise. Their spatial distribution, particularly the distance between two consecutive vortices along the mean flow direction,

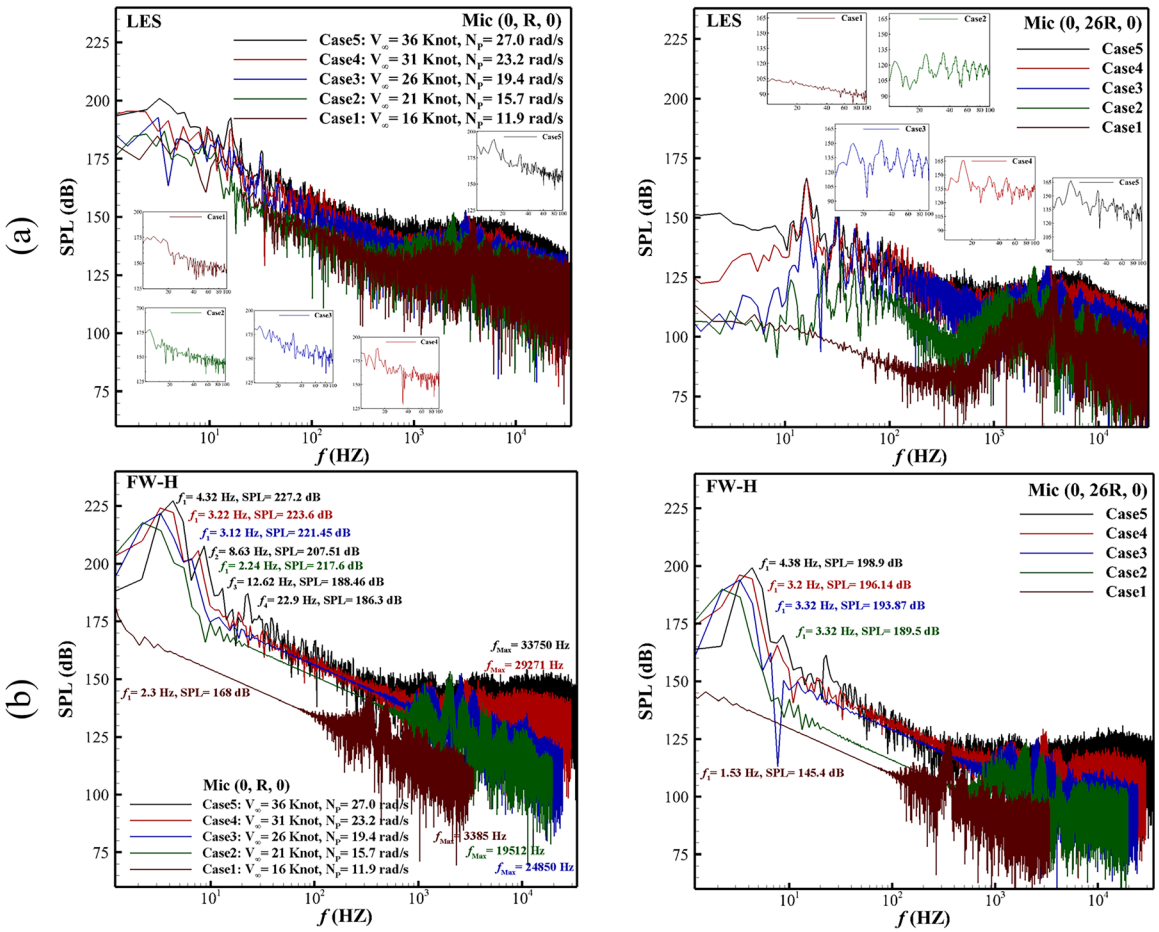

FIG. 20. Sound spectrum levels obtained using the FW-H and LES methods vary across different microphone locations, microphones at the radial points of $r_1 = 0R$; (a) LES, and (b) FW-H.

corresponds to the low frequencies observed in the SPL spectrum [see Figs. 20(b) and 21(b)]. In simpler terms, the decline in the signal related to the non-linear terms with distance is slower than of the linear terms.

Figure 20(b) also presents the frequencies of notable peaks in the acoustic spectra. The peak SPL, determined by the FW-H method, exhibit significant differences between cases, with the difference exceeding one order of magnitude between FSMV-case5 and FSMV-case1. For instance, the peak on the frequency spectrum of the FW-H method for FSMV-case5 reaches 203.6 dB, whereas the peak for FSMV-case1 is slightly below 150 dB at Mic (0, 14R, 0). The peaks and averages identified through LES exhibit lower dominant and higher average frequencies in compared to those obtained with the FW-H method. Moreover, the frequency spectrum appears to be broader, featuring smoother distributions.

To accurately evaluate the precise impact of cavitation noise on the distribution of the SPL, FSMV-case5 is replicated with the cavitation model deactivated (i.e., with the vapor volume fraction fixed at 0). Figure 22 plots the frequency domain representation of SPL for Mic_1 (0, R, 0) and Mic_2 (0, 6R, 0) between the cavitating and non-cavitating flow. Tip and hub vortex cavitation play a significant role in the continuous part of the noise spectrum and are particularly crucial in the low-frequency range. The increased noise attributed to the cavitation phenomenon occurring over the propeller is evident at low frequencies, whereas the noise levels at medium to high frequencies are relatively consistent. The results indicate that the OSPL is 12.02 dB louder at Mic1 (0, R, 0) and 8.35 dB louder at Mic2 (0, 6R, 0) in the cavitating case compared to the non-cavitating variant of case 5 (see Fig. 22).

The overall sound pressure level $[OSPL = 10.\log_{10}\left(\frac{1}{N}\sum_{i=1}^{N} 10^{\frac{SPL_i}{10}}.\Delta t\right)]$ at the specified microphone positions is depicted as a histogram in Fig. 23. A notable decrease in OSPL with increasing distance is evident, although it follows a nonlinear pattern. This nonlinearity can be attributed to the diminishing flow gradient, as discussed in the vorticity distribution section above, particularly at greater distances. For instance, in FSMV-case5, the OSPLs recorded at the axial position of Mic_2 (0, 6R, 0.9R) are approximately 11.54 dB higher than those at Mic_6 (0, 26R, 0). Notably, a significantly elevated noise level is detected at the location between the propeller hub and rudder leading edge, Mic_1 (0, R, 0). Specifically, in FSMV-case5, this

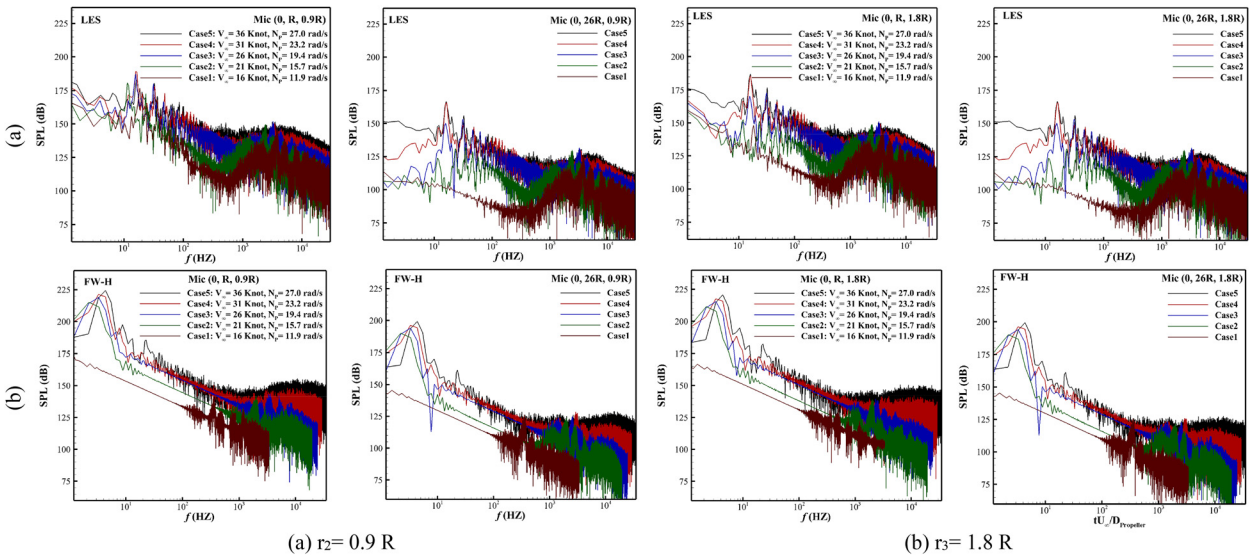

FIG. 21. Sound spectrum levels obtained using the FW-H and LES methods vary across different microphone locations, microphones at the radial points of (a) $r_2 = 0.9R$ and (b) $r_3 = 1.8R$.

microphone's recorded value of 140.69 dB is roughly 24 dB louder than the measurement obtained from the more distant Mic_6 (0, 26R, 0). Similar trends are observed at other radial positions, with a slightly reduced loudness of around 1.5 dB toward points farther away from the propeller. It can be inferred that the SPL exhibits a notable change in the axial direction and a smaller change radial direction within the near field. The comparison of OSPL obtained by high-fidelity LES modeling and FW-H method shows a slightly larger value for LES in almost all microphones. For instance, the average of deviation for microphones in three radial lines of FSMV-case5 at $r = 0$, 0.9R, and 1.8R are 3.16%, 2.07%, and 1.47%, respectively.

C. Power spectral density (PSD) analysis in the wake

The power spectral density (PSD) evolution can help explore the mechanism of energy transfer processes during propeller wake evolution that involves the fundamental frequencies wake evolution. PSDs for the time-history of streamwise pressure at several probes positioned downstream of the propellers are described in Figs. 24 and 25. The notable distinctions in the integral, inertial, and dissipative scales among different cases will be addressed here. Although the blade passage peak frequency is captured, the PSD reflects smaller frequency fluctuations dominated by the dynamics of the tip, root, trailing edge, and hub vortices, which are major structures shed by the propeller. These distributions contribute to both broadband and tonal frequencies, with the most energetic frequencies falling within the low range of frequencies. The following highlights are extracted from the spectral analysis of these figures:

(1) The adopted grid and time resolution are sufficiently fine to accurately capture and reproduce the complex turbulence behavior, as evidenced by a broad inertial range, even at the furthest downstream location ($L = 26R$).
(2) Because of the heightened instability of the tip and hub vortices downstream of the propeller, particularly in cases with higher N_P (FSMV_case3–5), the slope for the isotropic homogeneous

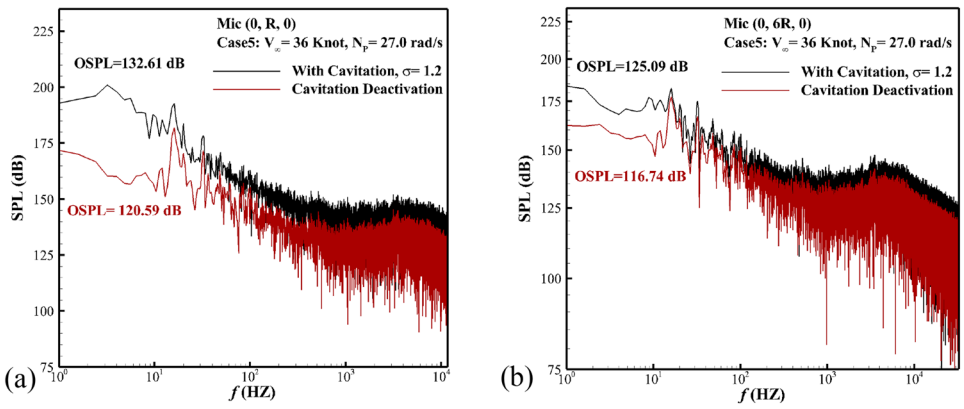

FIG. 22. Frequency domain comparison between cavitating and non-cavitating conditions, case 5 at (a) Mic (0, R, 0), (b) Mic (0, 6R, 0).

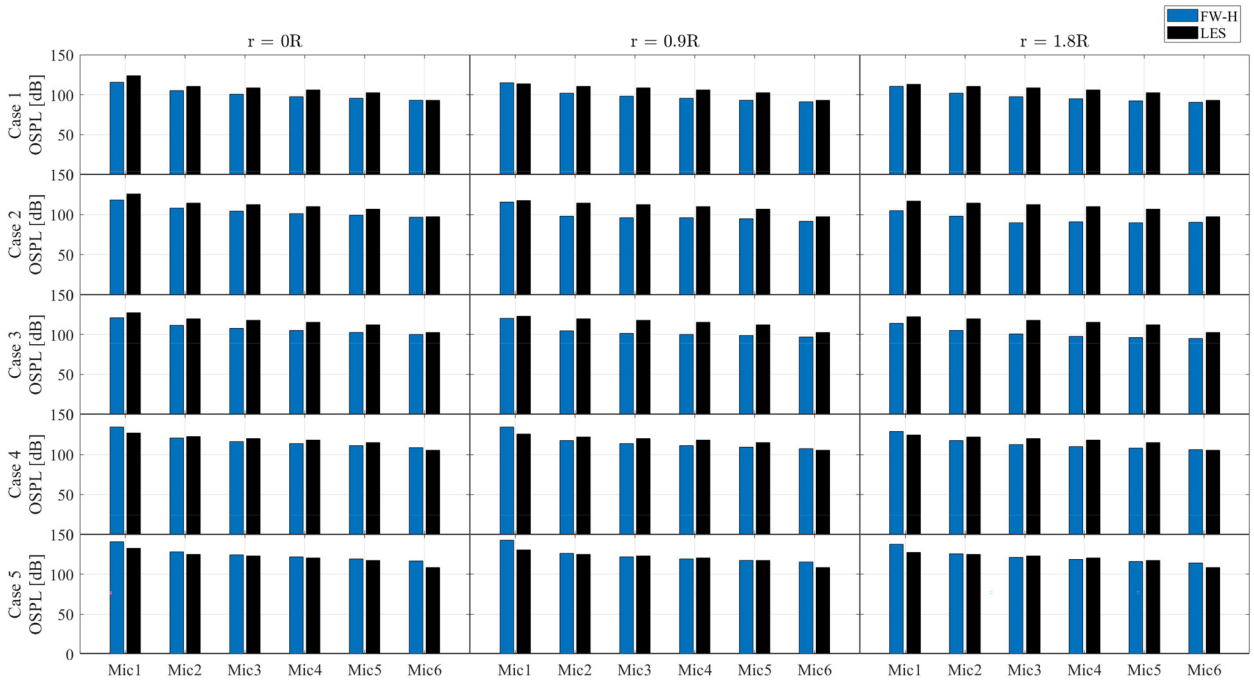

FIG. 23. Comparison between the OSPL for the FSMV cases, at $r_1 = 0R$, $r_2 = 0.9R$, and $r_3 = 1.8R$.

turbulence conforms to Kolmogorov's theory power law-decay ($f^{-5/3}$) scaling.

(3) Turbulence levels at both integral (low) and inertial (intermediate) frequencies are observed to decrease along the streamwise direction behind the propeller, attributable to the de-escalating instability of the vortical structures. Significant turbulence levels across all frequencies are evident for the microphones positioned between the rudder and propeller at L = R (see Fig. 24).

(4) A significant increase in the low frequency noise emanating from the hub vortex is observed for the microphones positioned at r = 0 (refer to Fig. 25). However, it is noteworthy that the instability at this zero radial distance r = 0 progresses at a slower rate than the influence of tip vortices at r = 0.9R.

(5) In this LES solution, the amplitudes of pressure PSDs gradually decrease as the microphones move downstream in all cases, attributed to energy dissipation during the evolution of tip vortices. The shrinkage of the spectra amplitude is visible across all frequency ranges.

The PSDs at rotating probes with propeller blades, which are dispersed along the radial direction, are shown in Fig. 26. The most significant levels in the frequencies' inertial range are observed at around r = 0.8–0.95R because of the tip vortices' instability, which starts the process of energy cascading from large to small scales. Due to the contraction experienced by the generated propeller wake at higher N_P, the highest PSD level shifts from the blade tip toward the negative radial

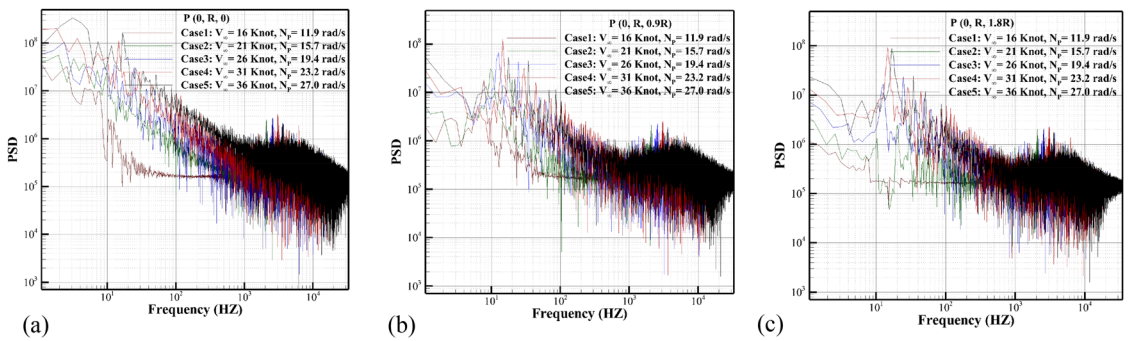

FIG. 24. Illustration of the PSD of the time-history of streamwise pressure at probes positioned at L = R and radial coordinate: (a) r = 0, (b) r = 0.9R, (c) r = 1.8R.

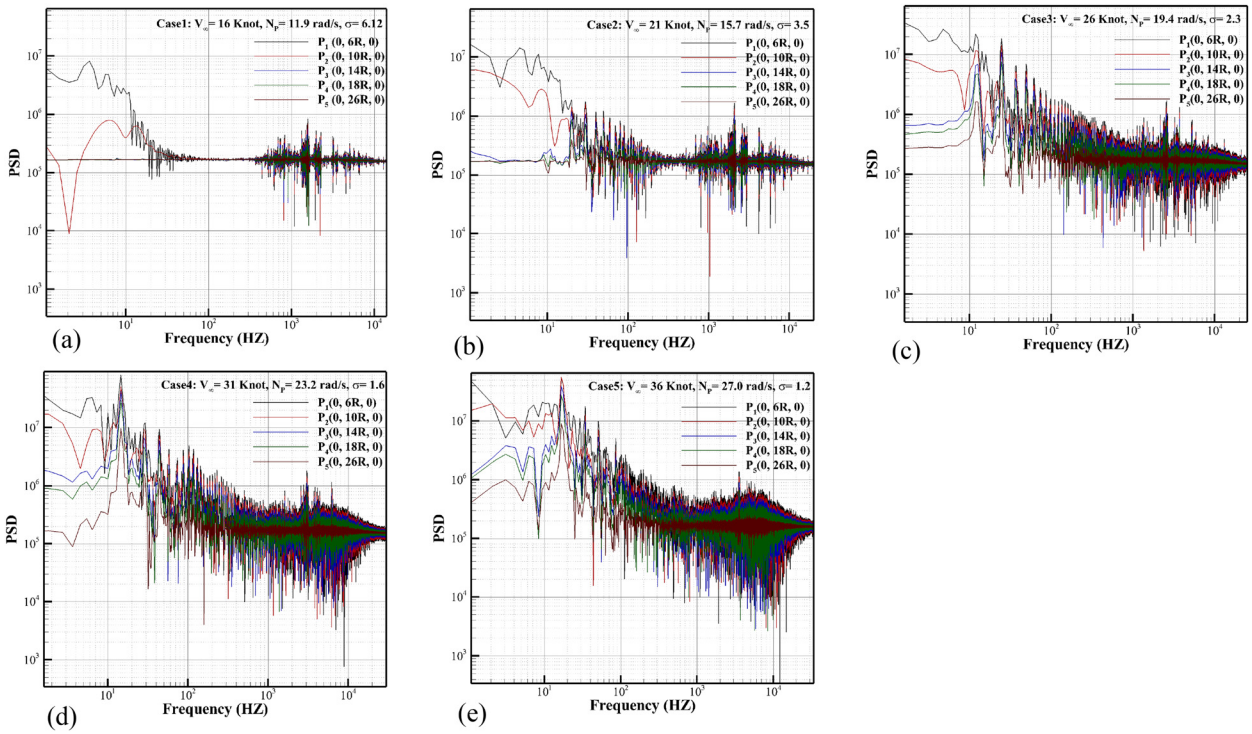

FIG. 25. Illustration of the PSD of the time-history of streamwise pressure at probes positioned at radial coordinate r = 0: FSMV (a) case 1, (b) case 2, (c) case 3, (d) case 4, and (e) case 5.

directions. Then, moving toward smaller radii, the PSD values decrease due to the decrement of the reduction in the prevalence of tip vortices, which serve as a primary source of turbulence instability, particularly affecting the outer boundary of the propeller wake.

The cavitation volume frequency spectrum is crucial for subsequent noise radiation analysis and more intense intermittent cavitation results in more pronounced noise radiation. Figure 27 depicts the frequency spectrum of the vapor volume fractions (α_v), for microphones considered in Fig. 17, which rotate together with the blade, a crucial factor for subsequent noise calculations. From this figure, it becomes evident that the harmonic fluctuations in cavity volume for two probes, located at the tip and 0.95R of the leading edge, are quite different, as are the behaviors observed in each case. The strongest frequency related to the cavitation volume fluctuation for FSMV_case5 at $\sigma = 1.2$ is f = 5.85 Hz, which is larger in magnitude than FSMV_case2, where f = 2.2 Hz. The reduction in low-frequency cavity fluctuations by decreasing the cavitation number and growth of the consequent cavitation number can be attributed to the effect of the contra-rotating system. The PSD of volume fluctuation at the blade leading edge (r = 0.95) as depicted in Fig. 27(b) is not greatly affected by variations in the cavitation number during various operational conditions.

VI. CONCLUDING REMARKS

A high-fidelity CFD analysis of a marine propeller was conducted to characterize turbulent wake structures under cavitating flow, aiming to reduce hydro-acoustic noise while maintaining propulsive

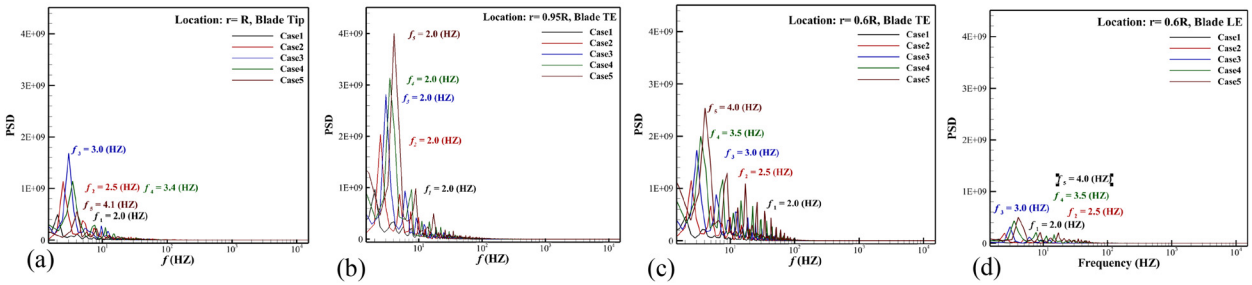

FIG. 26. Illustration of the PSD of the time-history of streamwise pressure for rotating probes positioned at different locations on the propeller blade surface: FSMV (a) blade tip r = R, (b) r = 0.95R TE, (c) r = 0.6R TE, and (d) r = 0.6R LE.

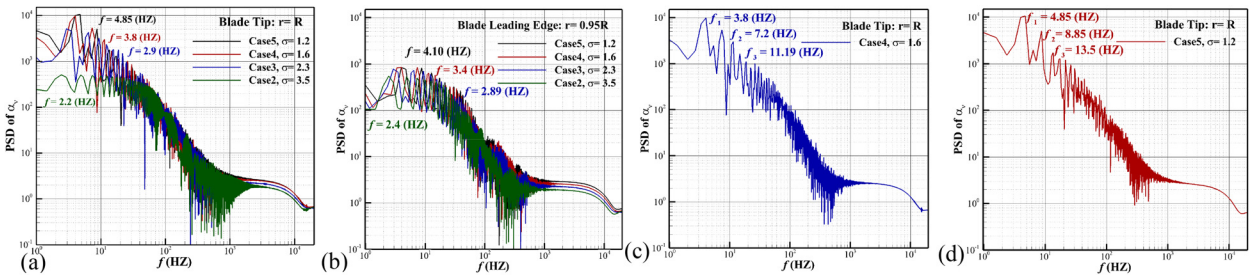

FIG. 27. Frequency spectrum of the vapor volume fractions (α_v): (a) r = R, (b) r = 0.95R, (d) FSMV_case4, r = R, (e) FSMV_case5, r = R.

efficiency. A full-scale marine vessel and a model-scale marine propeller (INSEAN E779A) with moving rudder were examined. Insights were gained to enhance propulsive efficiency and reduce noise by manipulating operational parameters such as propeller advance coefficient and cavitation number. A summary of the main conclusions from the investigations is provided below:

1. A detailed classification and delineation of the main hub, tip, root, and trailing edge vortical systems into the stable (region A), the transient (region B), and the unstable (region C) regimes is presented. The dominant vortical structures of the regions A, B, and C are the formation of the spiral tip vortices, diminishing of the gap between the adjacent tip vortices and formation of the complex small-scale vortices, respectively.
2. The overall expansion and fluctuation of wake structures, resulting from their oscillation and breakup, is observed with increasing propeller load. Additionally, in all operational conditions, both the hub and the tip vortices experience radial expansion in the downstream direction due to the energy dissipation of helical wake structures. The inner wake exhibits a notable velocity deficit, particularly pronounced within the hub vortex region, resulting in a downstream expansion.
3. Intensified swirling flow alters the structure of the tip, the root, the trailing edge, and the hub vortices, leading to a rapid reorganization and recirculation, transforming them into smaller scale vortical structures. Under these conditions, short-standing wake flow features involve the roll-up of the shear layers shed by the blades, generating multiple vortices across the span of the wake. The direct manifestation of these turbulent flow features is evident in the computed radiated sound levels.
4. Distinct cavitation types reproduced by the current LES modeling, i.e., sheet cavitation, tip cavitation, and hub cavitation, experience significant expansion with the increase of the rotational speed. Dethatched cavities directly manifest themselves in the computed the noise intensity, affecting multiple frequency ranges.
5. The thrust-to-torque coefficient ratio (K_T/K_Q) remains nearly constant at 2.8 despite the rage of thrusts produced by the propeller under different loading conditions. Furthermore, the maximum axial flow velocity occurs at around 0.7R of the propeller, playing a crucial role in generating thrust.
6. A quantitative analysis of pressure fluctuations around the propeller reveals a notable intensification during high blade loading, primarily attributed to the vortical structures and the cavitation development. The analysis of pressure fluctuations on the suction side of the blades also demonstrates substantial fluctuation due to the non-uniform wake distribution upstream of the propeller. The highest values pressure are achieved at around r = 0.6R to 0.8R due to intense tip vortex instability.
7. The peak and the average sound pressure levels (SPL) obtained through LES exhibit lower dominant and higher average frequencies in compared to those obtained using the FW-H equation. Furthermore, it can be inferred that the SPL of the FSMV exhibits moderate and slight spatial anisotropy in the axial and the radial directions, respectively.
8. The dominant spectral features of the acoustic signatures were concentrated in the low-frequency ($\leq$100 Hz) regimes, attributed to energetic helical vortices. At the frequencies exceeding 200 Hz, the frequency spectra exhibit smoother features. Narrow-band peaks in the medium-high frequency range originate from general sources, e.g., cavitation structures, background noise, or artifacts resulting from filtering.
9. Comparisons of OSPL obtained by the LES modeling and the FW-H method showed a higher predicted value for LES for almost all microphones. For instance, the average of the deviation for all receivers at r = 0, 0.9R, and 1.8R lines of FSMV-case5 were 3.16%, 2.07%, and 1.47%, respectively. Also, a notable nonlinear decrease in OSPL is evident with increasing distance from the propeller noise source. For instance, in FSMV-case5, the OSPLs at the Mic_1 (0, R, 0.9R) are around 24 dB higher than at the Mic_6 (0, 26R, 0).
10. The tip and the hub cavities contribute significantly to broadband noise and are particularly crucial in the low-frequency range. For instance, the OSPL for FSMV-case5 at Mic_1 (0, R, 0) under the cavitation operational conditions is 12.02 dB louder compared to the non-cavitating condition.

ACKNOWLEDGMENTS

The authors gratefully acknowledge the support of Transport Canada under the Quiet Vessel Initiative, the Natural Sciences and Engineering Research Council of Canada (NSERC), and the Digital Research Alliance of Canada and the University of Victoria under the Aspiration fellowship program.

AUTHOR DECLARATIONS

Conflict of Interest

The authors have no conflicts to disclose.

Author Contributions

Mohammad-Reza Pendar: Conceptualization (lead); Data curation (lead); Formal analysis (lead); Investigation (lead); Methodology (lead); Supervision (lead); Validation (lead); Visualization (lead); Writing – original draft (lead); Writing – review & editing (lead). **Duncan McIntyre:** Writing – review & editing (equal). **Peter Oshkai:** Funding acquisition (lead); Project administration (lead); Supervision (lead); Writing – review & editing (equal).

DATA AVAILABILITY

The data that support the findings of this study are available on request from the authors.

REFERENCES

Aktas, B., Atlar, M., Turkmen, S., Shi, W., Sampson, R., Korkut, E., and Fitzsimmons, P., "Propeller cavitation noise investigations of a research vessel using medium size cavitation tunnel tests and full-scale trials," Ocean Eng. **120**, 122–135 (2016).

Andrew, R. K., Howe, B. M., Mercer, J. A., and Dzieciuch, M. A., "Ocean ambient sound: Comparing the 1960s with the 1990s for a receiver off the California coast," Acoust. Res. Lett. **3**(2), 65–70 (2002).

Bensow, R., Bark, G., and Lu, N. X., "Hydrodynamic mechanisms in cavitation erosion," in 8th International Symposium on Cavitation, 2012.

Bensow, R. E. and Fureby, C., "On the justification and extension of mixed models in LES," J. Turbul. **8**, N54 (2007).

Bensow, R. and Liefvendahl, M., "An acoustic analogy and scale-resolving flow simulation methodology for the prediction of propeller radiated noise," in *31st Symposium on Naval Hydrodynamics* (US Office of Naval Research, 2016), pp. 11–16.

Bertschneider, H., Bosschers, J., Choi, G. H., Ciappi, E., Farabee, T., Kawakita, C., and Tang, D., "Specialist committee on hydrodynamic noise," in *Final Report and Recommendations to the 27th ITTC, Copenhagen, Sweden* (ITTC Association, 2014), p. 45.

Brentner, K. S. and Farassat, F., "Modeling aerodynamically generated sound of helicopter rotors," Prog. Aerosp. Sci. **39**(2–3), 83–120 (2003).

Chen, X., Sandham, N. D., and Zhang, X., "Cavity flow noise predictions," Technical Report No. AFM-07/05 (Aerodynamics & Flight Mechanics Group, University of Southampton, 2007).

Colonius, T. and Lele, S. K., "Computational aeroacoustics: Progress on nonlinear problems of sound generation," Prog. Aerosp. Sci. **40**(6), 345–416 (2004).

Crighton, D. G., Dowling, A. P., Ffowcs-Williams, J. E., Heckl, M., Leppington, F. G., and Bartram, J. F., *Modern Methods in Analytical Acoustics Lecture Notes* (Springer, 1992).

Di Francescantonio, P., "A new boundary integral formulation for the prediction of sound radiation," J. Sound Vib. **202**(4), 491–509 (1997).

Ebrahimi, A., Tootian, A., and Seif, M. S., "The effect of different endplate geometries on the hydrodynamic and acoustic performance of the tip-loaded propeller," Ocean Eng. **272**, 113885 (2023).

Ewert, R., "Broadband slat noise prediction based on CAA and stochastic sound sources from a fast random particle-mesh (RPM) method," Comput. Fluids **37**(4), 369–387 (2008).

Ewert, R., Dierke, J., Siebert, J., Neifeld, A., Appel, C., Siefert, M., and Kornow, O., "CAA broadband noise prediction for aeroacoustic design," J. Sound Vib. **330**(17), 4139–4160 (2011).

Farassat, F. and Myers, M. K., "Extension of Kirchhoff's formula to radiation from moving surfaces," J. Sound Vib. **123**(3), 451–460 (1988).

Felli, M., Camussi, R., and Di Felice, F., "Mechanisms of evolution of the propeller wake in the transition and far fields," J. Fluid Mech. **682**, 5–53 (2011).

Felli, M., Falchi, M., and Dubbioso, G., "Tomographic-PIV survey of the near-field hydrodynamic and hydroacoustic characteristics of a marine propeller," J. Ship Res. **59**(04), 201–208 (2015).

Ghosal, S., "An analysis of numerical errors in large-eddy simulations of turbulence," J. Comput. Phys. **125**, 187–206 (1996).

Gorji, M., Ghassemi, H., and Mohamadi, J., "Effect of rake and skew on the hydrodynamic characteristics and noise level of the marine propeller," Iranian J. Sci. Technol. Trans. Mech. Eng. **43**, 75–85 (2019).

Guo, Y., "A semi-empirical model for aircraft landing gear noise prediction," AIAA Paper No. 2006-2627, 2006.

Hildebrand, J. A., "Anthropogenic and natural sources of ambient noise in the ocean," Mar. Ecol. Prog. Ser. **395**, 5–20 (2009).

Houser, D. S., Mulsow, J., Branstetter, B., Moore, P. W., Finneran, J. J., and Xitco, M. J., "The characterisation of underwater noise at facilities holding marine mammals," Anim. Welfare **28**(2), 143–155 (2019).

Hu, J., Ning, X., Zhao, W., Li, F., Ma, J., Zhang, W., Sun, S., Zou, M., and Lin, C., "Numerical simulation of the cavitating noise of contra-rotating propellers based on detached eddy simulation and the Ffowcs Williams–Hawkings acoustics equation," Phys. Fluids **33**(11), 115117 (2021).

Hunt, J. C., Wray, A. A., and Moin, P., "Eddies, streams, and convergence zones in turbulent flows. Studying turbulence using numerical simulation databases," in Proceedings of the 1988 Summer Program, 1988.

Ianniello, S., "The Ffowcs Williams–Hawkings equation for hydroacoustic analysis of rotating blades. Part I. The rotpole," J. Fluid Mech. **797**, 345–388 (2016).

Ianniello, S. and De Bernardis, E., "Farassat's formulations in marine propeller hydroacoustics," Int. J. Aeroacoust. **14**(1–2), 87–103 (2015).

Ianniello, S., Muscari, R., and Di Mascio, A., "Ship underwater noise assessment by the acoustic analogy. Part I: Nonlinear analysis of a marine propeller in a uniform flow," J. Mar. Sci. Technol. **18**, 547–570 (2013).

Ianniello, S., Muscari, R., and Di Mascio, A., "Ship underwater noise assessment by the acoustic analogy part II: Hydroacoustic analysis of a ship scaled model," J. Mar. Sci. Technol. **19**, 52–74 (2014).

Ianniello, S. and Testa, C., "An overview on the use of the Ffowcs Williams-Hawkings equation for the hydroacoustic analysis of marine propellers," in *MARINE VIII: Proceedings of the VIII International Conference on Computational Methods in Marine Engineering* (CIMNE, 2019), pp. 99–110.

IMO, M., *Guidelines for the Reduction of Underwater Noise from Commercial Shipping to Address Adverse Impacts on Marine Life* (MEPC, 2014).

Ji, B., Luo, X., Wu, Y., Peng, X., and Xu, H., "Partially-averaged Navier–Stokes method with modified k–ε model for cavitating flow around a marine propeller in a non-uniform wake," Int. J. Heat Mass Transfer **55**(23–24), 6582–6588 (2012).

Kowalczyk, S. and Felicjancik, J., "Numerical and experimental propeller noise investigations," Ocean Eng. **120**, 108–115 (2016).

Ku, G., Cho, J., Cheong, C., and Seol, H., "Numerical investigation of tip-vortex cavitation noise of submarine propellers using hybrid computational hydroacoustic approach," Ocean Eng. **238**, 109693 (2021).

Kurbatskii, K. A. and Mankbadi, R. R., "Review of computational aeroacoustics algorithms," Int. J. Comput. Fluid Dyn. **18**(6), 533–546 (2004).

Li, Z., Qian, Z., and Ji, B., "Transient cavitating flow structure and acoustic analysis of a hydrofoil with whalelike wavy leading edge," Appl. Math. Modell. **85**, 60–88 (2020).

Lidtke, A. K., Humphrey, V. F., and Turnock, S. R., "Feasibility study into a computational approach for marine propeller noise and cavitation modelling," Ocean Eng. **120**, 152–159 (2016a).

Lidtke, A. K., Turnock, S. R., and Humphrey, V. F., "Characterisation of sheet cavity noise of a hydrofoil using the Ffowcs Williams–Hawkings acoustic analogy," Comput. Fluids **130**, 8–23 (2016b).

Lighthill, M. J., "On sound generated aerodynamically I. General theory," Proc. R. Soc. London, Ser. A **211**(1107), 564–587 (1952).

Lloyd, T., Rijpkema, D., and van Wijngaarden, E., "Marine propeller acoustic modelling: Comparing CFD results with an acoustic analogy method," in Fourth International Symposium on Marine Propulsors, Austin, Texas, 2015.

Long, Y., Long, X. P., Ji, B., Huai, W. X., and Qian, Z. D., "Verification and validation of URANS simulations of the turbulent cavitating flow around the hydrofoil," J. Hydrodyn. **29**(4), 610–620 (2017).

McDonald, M. A., Hildebrand, J. A., and Wiggins, S. M., "Increases in deep ocean ambient noise in the Northeast Pacific west of San Nicolas Island, California," J. Acoust. Soc. Am. **120**(2), 711–718 (2006).

McKenna, M. F., Ross, D., Wiggins, S. M., and Hildebrand, J. A., "Underwater radiated noise from modern commercial ships," J. Acoust. Soc. Am. **131**(1), 92–103 (2012).

Mendez, S., Shoeybi, M., Lele, S. K., and Moin, P., "On the use of the Ffowcs Williams-Hawkings equation to predict far-field jet noise from large-eddy simulations," Int. J. Aeroacoust. **12**(1–2), 1–20 (2013).
Pan, Y. C. and Zhang, H. X., "Numerical prediction of marine propeller noise in non-uniform inflow," China Ocean Eng. **27**, 33–42 (2013).
Pendar, M. R., Alavi, A., and Roohi, E., "Identification of frequency modes and spectral content for noise suppression: Cavitation flow over 3-D hydrofoil with sinusoidal leading edge," Int. J. Mod. Phys. C **34**(06), 2350074 (2023a).
Pendar, M. R., Candido, S., and Pascoa, J. C., "Optimization of painting efficiency applying unique techniques of high-voltage conductors and nitrotherm spray: Developing deep learning models using computational fluid dynamics dataset," Phys. Fluids **35**(7), 075119 (2023b).
Pendar, M. R., Esmaeilifar, E., and Roohi, E., "LES study of unsteady cavitation characteristics of a 3-D hydrofoil with wavy leading edge," Int. J. Multiphase Flow **132**, 103415 (2020).
Pendar, M. R. and Pascoa, J. C., "Numerical modeling of electrostatic spray painting transfer processes in rotary bell cup for automotive painting," Int. J. Heat Fluid Flow **80**, 108499 (2019).
Pendar, M. R. and Pascoa, J., "Study of the plasma actuator effect on the flow characteristics of an airfoil: An LES investigation," SAE Int. J. Adv. Curr. Pract. Mobility **3**, 1206–1215 (2021).
Pendar, M. R. and Roohi, E., "Cavitation characteristics around a sphere: An LES investigation," Int. J. Multiphase Flow **98**, 1–23 (2018).
Plesset, M. S. and Prosperetti, A., "Bubble dynamics and cavitation," Annu. Rev. Fluid Mech. **9**(1), 145–185 (1977).
Poinsot, T. J. A. and Lelef, S. K., "Boundary conditions for direct simulations of compressible viscous flows," J. Comput. Phys. **101**(1), 104–129 (1992).
Popper, A. N. and Hawkins, A., *The Effects of Noise on Aquatic Life II* (Springer, New York, 2016), Vol. 875.
Posa, A., Broglia, R., and Felli, M., "Acoustic signature of a propeller operating upstream of a hydrofoil," Phys. Fluids **34**(6), 065132 (2022).
Razaghian, A. H., Ebrahimi, A., Zahedi, F., Javanmardi, M. R., and Seif, M. S., "Investigating the effect of geometric parameters on hydrodynamic and hydroacoustic performances of submerged propellers," Appl. Ocean Res. **114**, 102773 (2021).
Rudy, D. H. and Strikwerda, J. C., "A nonreflecting outflow boundary condition for subsonic Navier–Stokes calculations," J. Comput. Phys. **36**(1), 55–70 (1980).
Salvatore, F., Streckwall, H., and Van Terwisga, T., "Propeller cavitation modelling by CFD-results from the VIRTUE 2008 Rome workshop," in *Proceedings of the First International Symposium on Marine Propulsors, Trondheim, Norway* (Norwegian Marine Technology Research Institute, 2009), pp. 22–24.
Salvatore, F., Testa, C., Ianniello, S., and Pereira, F., "Theoretical modelling of unsteady cavitation and induced noise," in *Proceedings of CAV 2006 Symposium* (Maritime Research Institute Netherlands, 2006), pp. 1–13.
Sauer, J., "Instationaren Kaviterende Stromung-Ein Neues Modell, Baserend Auf Front Capturing (VOF) and Blasendynamik," Ph.D. thesis (University of Karlsruhe, 2000).
Schnerr, G. H. and Sauer, J., "Physical and numerical modeling of unsteady cavitation dynamics," in Proceedings of 4th International Conference on Multiphase Flow, New Orleans, USA, 2001.
Seol, H., Suh, J. C., and Lee, S., "Development of hybrid method for the prediction of underwater propeller noise," J. Sound Vib. **288**(1–2), 345–360 (2005).
Sezen, S., Atlar, M., Fitzsimmons, P., Sasaki, N., Tani, G., Yilmaz, N., and Aktas, B., "Numerical cavitation noise prediction of a benchmark research vessel propeller," Ocean Eng. **211**, 107549 (2020).
Sezen, S., Cosgun, T., Yurtseven, A., and Atlar, M., "Numerical investigation of marine propeller underwater radiated noise using acoustic analogy Part 2: The influence of eddy viscosity turbulence models," Ocean Eng. **220**, 108353 (2021).
Spalart, P. R., Belyaev, K. V., Shur, M. L., Kh Strelets, M., and Travin, A. K., "On the differences in noise predictions based on solid and permeable surface Ffowcs Williams–Hawkings integral solutions," Int. J. Aeroacoust. **18**(6–7), 621–646 (2019).
Tam, C. K., "Computational aeroacoustics: An overview of computational challenges and applications," Int. J. Comput. Fluid Dyn. **18**(6), 547–567 (2004).
Tam, C. K. and Webb, J. C., "Dispersion-relation-preserving finite difference schemes for computational acoustics," J. Comput. Phys. **107**(2), 262–281 (1993).
Tani, G., Aktas, B., Viviani, M., Yilmaz, N., Miglianti, F., Ferrando, M., and Atlar, M., "Cavitation tunnel tests for "The Princess Royal" model propeller behind a 2-dimensional wake screen," Ocean Eng. **172**, 829–843 (2019).
Tani, G., Villa, D., Gaggero, S., Viviani, M., Ausonio, P., Travi, P., Bizzarri, G., and Serra, F., "Experimental investigation of pressure pulses and radiated noise for two alternative designs of the propeller of a high-speed craft," Ocean Eng. **132**, 45–69 (2017).
Testa, C., Porcacchia, F., Zaghi, S., and Gennaretti, M., "Study of a FWH-based permeable-surface formulation for propeller hydroacoustics," Ocean Eng. **240**, 109828 (2021).
Thompson, K. W., "Time dependent boundary conditions for hyperbolic systems," J. Comput. Phys. **68**(1), 1–24 (1987).
Turner, J. M. and Kim, J. W., "On the universal trends in the noise reduction due to wavy leading edges in aerofoil–vortex interaction," J. Fluid Mech. **871**, 186–211 (2019).
Ubbink, O., "Numerical prediction of two fluid systems with sharp interfaces," *Ph.D. dissertaion* (University of London, 1997).
Viitanen, V. M., Hynninen, A., Sipilä, T., and Siikonen, T., "DDES of wetted and cavitating marine propeller for CHA underwater noise assessment," J. Mar. Sci. Eng. **6**(2), 56 (2018).
Wang, C., Huang, B., Wang, G., Zhang, M., and Ding, N., "Unsteady pressure fluctuation characteristics in the process of breakup and shedding of sheet/cloud cavitation," Int. J. Heat Mass Transfer **114**, 769–785 (2017).
Wang, L., Wu, T., Gong, J., and Yang, Y., "Numerical analysis of the wake dynamics of a propeller," Phys. Fluids **33**(9), 095120 (2021).
Wang, Y., He, C., Wang, X., Cheng, H., and Ji, B., "Influence of skew angle on the cavitation dynamics and induced low-frequency pressure fluctuations around a marine propeller," Ocean Eng. **277**, 114302 (2023).
Wells, V. L. and Renaut, R. A., "Computing aerodynamically generated noise," Annu. Rev. Fluid Mech. **29**(1), 161–199 (1997).
Williams, J. F. and Hawkings, D. L., "Sound generation by turbulence and surfaces in arbitrary motion," Philos. Trans. R. Soc. London, Ser. A **264**, 321–342 (1969).
Witte, M., Hieke, M., and Wurm, F. H., "Identification of coherent flow structures and experimental analysis of the hydroacoustic emission of a hubless propeller," Ocean Eng. **188**, 106248 (2019).
Wittekind, D. and Schuster, M., "Propeller cavitation noise and background noise in the sea," Ocean Eng. **120**, 116–121 (2016).
Wu, Q., Huang, B., Wang, G., Cao, S., and Zhu, M., "Numerical modelling of unsteady cavitation and induced noise around a marine propeller," Ocean Eng. **160**, 143–155 (2018).
Yu, C., Wang, Y., Huang, C., Wu, X., and Du, T., "Large eddy simulation of unsteady cavitating flow around a highly skewed propeller in nonuniform wake," J. Fluids Eng. **139**(4), 041302 (2017).
Yu, K., Park, D., Choi, J., Seol, H., Park, I., and Lee, S., "Effect of skew on the tonal noise characteristics of a full-scale submarine propeller," Ocean Eng. **276**, 114218 (2023).